



HAL
open science

Numerical analysis of the effects of wrinkles in the radius of curvature of L-shaped CFRP specimens on unfolding failure

P. Journoud, Christophe Bouvet, Bruno Castanié, L. Ratsifandrihana

► To cite this version:

P. Journoud, Christophe Bouvet, Bruno Castanié, L. Ratsifandrihana. Numerical analysis of the effects of wrinkles in the radius of curvature of L-shaped CFRP specimens on unfolding failure. *Composite Structures*, 2022, 299, pp.116107. 10.1016/j.compstruct.2022.116107 . hal-03847451

HAL Id: hal-03847451

<https://hal.science/hal-03847451>

Submitted on 18 Nov 2022

HAL is a multi-disciplinary open access archive for the deposit and dissemination of scientific research documents, whether they are published or not. The documents may come from teaching and research institutions in France or abroad, or from public or private research centers.

L'archive ouverte pluridisciplinaire **HAL**, est destinée au dépôt et à la diffusion de documents scientifiques de niveau recherche, publiés ou non, émanant des établissements d'enseignement et de recherche français ou étrangers, des laboratoires publics ou privés.

Numerical analysis of the effects of wrinkles in the radius of curvature of L-Shaped CFRP specimens on unfolding failure

P. Journoud^{1,2}, C. Bouvet¹, B. Castanié¹, L. Ratsifandrihana²

1: Institut Clément Ader, Université de Toulouse, CNRS UMR 5312 – INSA – ISAE-SUPAERO – IMT Mines Albi – UPS – 3 rue Caroline Aigle, 31400 TOULOUSE, FRANCE

2 : Segula Aerospace & Defence, Segula Technologie – immeuble EQUINOX – bat. 1, 24 Boulevard Déodat de Severac, 31770 COLOMIERS, France

Abstract

Complex composite parts, and especially curved laminated composites, are more subject to defects than flat laminates. One of the most common defects is the presence of wrinkles, which can occur in the radius of curvature. Wrinkle effects must be studied to evaluate their influence on the mechanical properties of laminated composites. In this study, a numerical model was developed to take wrinkle and local delamination defects into consideration and assess their impact on the failure load of L-angle specimens under four-point bending tests. Experimental wrinkles based on a previous work were modelled using the Discrete Ply Model strategy and four-point bending simulations were run. The numerical model allowed the effects of each defect (local delamination and wrinkle) to be distinguished and their combined influence on the failure load to be studied with respect to the maximum misalignment.

Keywords: wrinkle defects, initial delamination defects, numerical model, composite L-angle, unfolding failure, translaminar matrix cracking, delamination

1. Introduction

By their construction, laminated composite materials have interesting stiffness and in plane strength-to-weight ratio, and can be used in many different design architectures [1]. However, with classical sandwich or laminate architectures, there are no reinforcements normal to the direction of the fibres. Therefore, loads through the thickness are a major weakness of laminated composite structures and delamination is a commonly observed type of failure. Delamination can be caused by high out-of-plane tensile stresses or interlaminar stresses developing at discontinuities and free edges [2,3]. Due to their geometry and, in particular, the radius of curvature, curved laminated composite structures are more subject to unfolding and consequently to through-the-thickness loading [4].

Unfolding failure due to delamination is commonly identified in highly curved laminated composites [5,6]. Many researchers have studied the mechanisms leading to the failure of specimens under out-of-plane loads. Olsson [7] provides an overview of the different test methods for multiaxial and out-of-plane strength of laminated composite specimens. Four-point bending tests present some advantages compared with other tests: the self-alignment of the specimen makes setup relatively simple and stress induced by the roller bearings is negligible [8]. Delamination failure of a unidirectional curved specimen in a four-point bending test is driven by interlaminar tensile strength. Jackson and Martin [9] demonstrated that interlaminar tensile strength was highly dependent on the laminate quality and on the presence of voids. Wisnom [10] evaluated the distribution of interlaminar tensile stress through the width of curved specimens and highlighted free edge effects. This result corroborates the works of Fletcher et al. [11,12]. Sun and Kelly [13,14] were among the first to study damage modes in cross-ply curved specimens in four-point bending tests. They demonstrated that the presence of 90° plies might modify the unfolding failure of the specimen, which can result from interactions between matrix cracking and delamination depending on the stacking sequence. More recently, Huchette et al. [15] and González-Cantero et al. [16] demonstrated that delaminations were due to interlaminar matrix cracking occurring first. Some authors [17,18] demonstrated that the interlaminar tensile strength was thickness dependent. Charrier et al. [18] studied four stacking sequences of L-angle specimens in particular with three different thicknesses under four-point bending loads and they concluded that interlaminar tensile strength decreased with increasing specimen thickness.

Some authors have used finite element methods to better understand the unfolding failure of curved laminated composites. Like Nguyen et al. [19], who used cohesive zones to model and evaluate the delamination of multi-angle curved specimens under four-point bending tests, most of them considered delamination. More recently, some works [20–23] have taken both interlaminar and intralaminar damage

into consideration for the failure of curved specimens and studied their interaction. They have shown that matrix cracking could effectively drive delamination and lead to the failure of the specimen in the case of multi-angle stacking sequences but, in the case of unidirectional layup, the unfolding failure was mainly due to interlaminar failure. In conclusion, the percentage and position of 90° plies have significant influence on the out-of-plane tensile strength of curved specimens under four-point bending tests.

Due to their complex geometry, curved laminated specimens are subject to many defects [24], the most common of which is out-of-plane wrinkling. Wrinkles have significant effects on mechanical properties. Most studies in the literature focus on out-of-plane wrinkle effects in the cases of in-plane tensile [25] and compressive strength [26–28]. To the best of the authors' knowledge, only two recent papers deal with the influence of wrinkles on the through-the-thickness tensile strength [29,30]. Xu et al. [30] conducted an experimental and numerical study of wrinkle effects on the out-of-plane tensile strength of an L-angle specimen under four-point bending. They focused on two layups, one of which, with a wrinkle angle of 18° calculated from the wavelength and the amplitude, led to a reduction of through-the-thickness tensile strength of 16%. They used the same method as Mukhopadhyay et al. [25,26] to introduce wrinkles. This consists of putting additional 90° strips of prepregs into the stacking sequence to force adjacent plies to wrinkle. Hu et al. [29] also conducted an experimental and numerical study of wrinkle effects on the failure load of curved specimens under bending tests. They produced wrinkled specimens without additional pieces of prepreg. Their method was first to make a pre-stacking layup on a flat tool before introducing it into the mould. They concluded that the amplitudes and locations of wrinkles had significant influence on mechanical response, leading to a reduction of 30-40% of the failure load. That was in agreement with the experimental results presented in a preceding work of the authors [31] on the effect of wrinkle defects on the out-of-plane strength of curved specimens under four-point bending tests.

The experimental basis of this study comes from the previous work of the authors [31] on experimental four point-bending tests on wrinkled specimens. Unfortunately, the experimental results did not distinguish between the influence of initial delamination and wrinkle defects. Therefore, it is important to develop a numerical model to understand the influence of each defect on the failure scenario of specimens with defects. This will make it possible to estimate the ultimate load of curved specimens numerically, with the aim of estimating the knockdown factor depending on the maximum misalignment. A first numerical model [22] based on a modelling strategy called DPM has already been used to simulate four-point bending tests on a curved specimen without defects. This numerical model was implemented within the Finite Element (FE) code Abaqus/Explicit [32]. This model gave good agreement between experimental and numerical simulations, especially for the Load – Machine Displacement curves and damage scenario. The numerical model was able to capture the maximal load, load drops and the different reaction loads for the

stacking sequences studied. For this reason, it will be adapted in this study to model wrinkles in curved specimens under four-point-bending tests.

Experimental wrinkles, presented in a previous study [31] are briefly recalled in Section 2. The tests and materials are recalled in section 3.1. The discrete ply model is briefly recalled in Section 3.2 and its adaptation for modelling wrinkles is introduced in Section 3.3. Section 4 focuses on three numerical simulations of specimens with different defects. The specimens studied in Section 4.1 present the specimen considered without wrinkles but which has local delamination defects. The case of Section 4.2 is a specimen with an intermediate level of wrinkles and without local delamination defects. Section 4.3 focuses on a specimen with a high level of wrinkles and with initial delamination defects. Section 4.4 deals with the numerical study of the variation of failure load in relation with the misalignment angle in two cases: with and without initial delamination defects. To finish, Section 4.5 presents a comparison between experimental and numerical failure loads for a large number of different misalignment angles. Finally, in Section 5, conclusions are drawn based on the above.

2. Experimental specimens studied

In this part, we briefly recall the manufactured specimens presented in [31] and present the geometry of the wrinkles modelled for this study. The manufacturing of these specimens was detailed in a previous study [31] and interested readers are invited to refer to this article for more information.

A total of 42 specimens, divided into 7 batches, were made by using two strategies of hand layup for the composite. The samples presented different levels of wrinkles, which were characterised by the maximum misalignment angle compared to the reference surface, with a range from $1.5\pm 2^\circ$ to $83\pm 2^\circ$. Images of specimens modelled in the study are presented in Fig. 1.

Previous work had highlighted the influence of wrinkles on the out-of-plane tensile strength of curved specimens under four-point bending tests. The length of initial delamination defects were studied but no relation could be established between this length and the failure load, probably because of a lack of information.

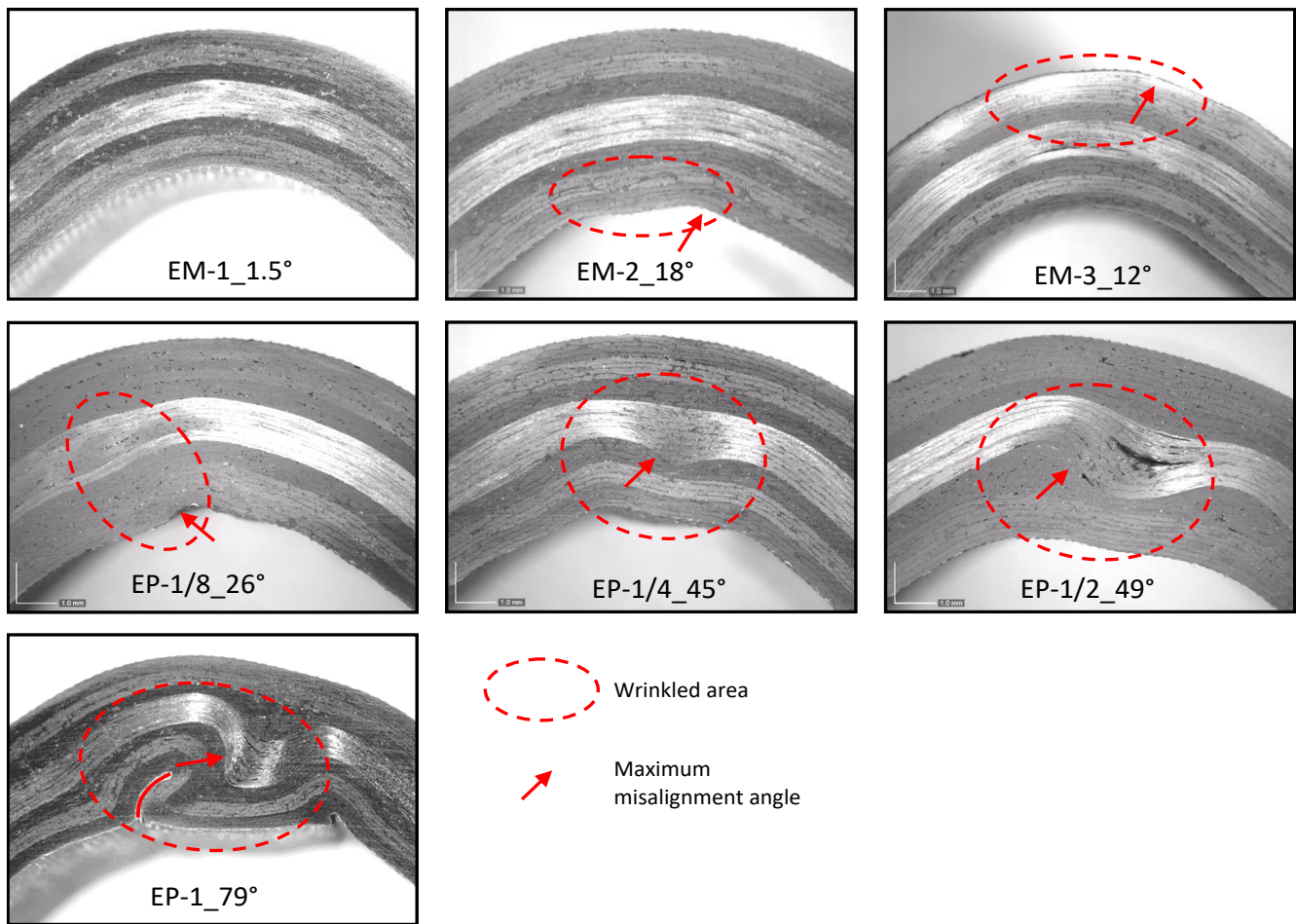


Fig. 1: Images of modelled specimens

3. Numerical modelling

In this section, the “Discrete Ply Model” (DPM) [22,33–35] is briefly recalled. The main advantages of this model are that it uses a continuum damage of fibre breaks and a discrete modelling of the delamination and matrix cracking. This model has been presented in more detail in previous papers [36,37]. Interested readers are invited to refer to them for further presentation. Materials and boundary conditions, involved in the modelling of various types of damage, and also the mesh strategy are then detailed respectively in sections 3.1, 3.2, and 3.3.

3.1. Materials and boundary conditions

The four-point bending test, schematised in Fig. 2, was used to study the unfolding failure of L-angle specimens. This test consists of inducing a bending moment by the displacement of the two upper

cylindrical rolling bars, while the two lower ones stay fixed. This loading tends to flatten the part and generate out-of-plane tensile stresses in the curvature. The geometry of the specimens was designed by Charrier et al. [18] to examine failure delamination by the minimisation of the out-of-plane shear stress and the maximisation of the out-of-plane tensile stress in the curvature of the sample. Interested readers may refer to [18] for more information about specimen design and characteristic parameters of the experimental devices of the four-point bending tests. The dimensions of the specimens are reported in Table 1.

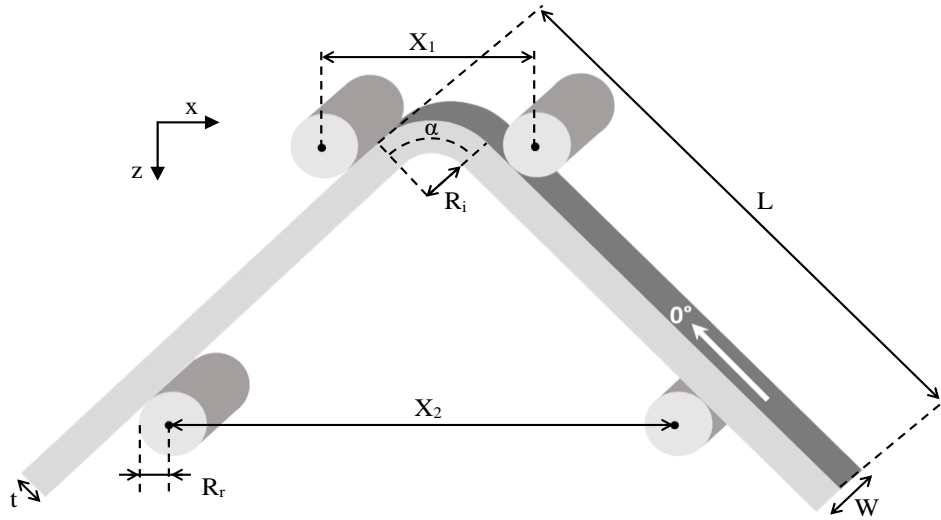


Fig. 2: Configuration of the four-point bending test on L-angle specimen

Table 1: Experimental setup characteristics, parameters, and L-angle specimen dimensions

Thickness	Length	Width	Inner radius	Radius of cylindrical bars	Loading bars	Support bars
t (mm)	L (mm)	w (mm)	R _i (mm)	R _r (mm)	X ₁ (mm)	X ₂ (mm)
4.125	113	20	5.16	7.5	30	66

Four-point bending tests were conducted on L-angle specimens made of T700GC/M21 carbon/epoxy laminated composite. A single stacking sequence was used in this study [45₂/-45₂/90₂/0₂]_s with a nominal ply thickness of 0.257 mm, leading to a theoretical global thickness of 4.125 mm. The longitudinal direction of the fibres is considered to be the along-the-length direction of the specimen (Fig. 2).

Boundary conditions were applied to loading and support bars. For the support bars, translations and rotation were permitted only along the axis of the cylinder. For the loading bars, displacements were imposed and rotation along the axis of the cylinder was allowed.

3.2. Modelling of various types of damage

Meshing Strategy:

A complex 3D mesh following the orientation of each ply was used on the DPM to simulate the different failure modes (Fig. 3.). Volume elements used for the fibre failure were C3D8 and C3D6 for all orientations [38]. Interface elements used for delamination and matrix cracking were classical cohesive zone model COH3D8 and COH3D6 elements. Interface elements used for matrix cracking were localised between two volume elements in the direction of the ply and interface elements used for delaminations were localised at the interface of two adjacent plies.

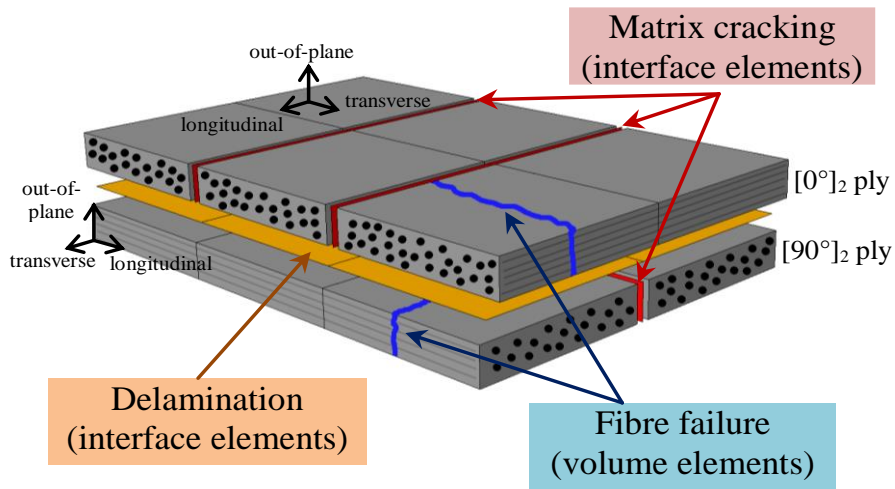


Fig. 3: Modelling of various damage with the DPM

Damage laws:

- A bilinear material law (Eq.1) considering the crack surface energy was used to calculate the continuum damage of the fibre at integration points of the volume element (illustrated in grey on Fig. 3).

$$\int_V \left(\int_0^{\varepsilon^1} \sigma_l d\varepsilon_l \right) \cdot dV = S \cdot G_{Ic}^{f,T} \quad (\text{Eq. 1})$$

where $G_{Ic}^{f,T}$ and $G_{Ic}^{f,C}$ are the critical energy release rate in opening mode in the fibre direction for the tensile case and for the compressive case respectively, σ_l and ε_l are the longitudinal stress and strain, ε^1 is the strain at total degradation of fibre stiffness, and V and S are the element volume and section. A damage variable, noted d , was used to take account of a linear decrease of the stress in tensile and compression fibre failure when the strain limits, ε_t^0 and ε_c^0 , were achieved.

- Interface elements were used between two consecutive plies (illustrated in orange in Fig. 3) to take account of delamination, which is directed by the dissipation energy of fracture mechanisms. The three modes of delamination are taken into account in the criterion (Eq. 2): the opening mode I, and shear modes II and III, which are not distinguished here. A linear law of mixed-mode delamination propagation with energy release in each mode was used in the present work.

$$\frac{G_I}{G_{Ic}^{del}} + \frac{G_{II}}{G_{IIc}^{del}} + \frac{G_{III}}{G_{IIIc}^{del}} = 1 \quad (\text{Eq. 2})$$

- Interface elements (illustrated in red in Fig. 3) between two adjacent volume elements are used to take matrix cracking into consideration. A Hashin's failure criterion (Eq. 3) was used to manage the damage of matrix cracking within the interface element.

$$\left(\frac{\sigma_t^+}{\sigma_t^f}\right)^2 + \frac{\tau_{lt}^2 + \tau_{tz}^2}{(\tau_{lt}^f)^2} \leq 1 \quad (\text{Eq. 3})$$

where σ_t^f and τ_{lt}^f are the transverse and shear failure stresses and (l, t, z) are respectively the longitudinal, transverse and out-of-plane directions.

In fine, this modelling strategy requires only 15 material parameters, which are listed in Table 2.

Table 2: Material properties used in the DPM Modelling

Density		1 600 Kg/m ³
Orthotropic elastic properties		
E_l^t	Tensile Young's modulus in fibre direction	130 000 MPa
E_l^c	Compressive Young's modulus in fibre direction	100 000 MPa
E_t	Transverse Young's Modulus	7 700 MPa
$G_{lt} = G_{lz}$	In-plane shear modulus	4 750 MPa
G_{tz}	Out-of-plane shear modulus	2 900 MPa
ν_{lt}	Poisson's ratio	0.3
Fibre failure		
σ^{crush}	Mean longitudinal compressive crushing stress	250 MPa
ε_t^0	Tensile strain in fibre direction at damage initiation	0.016
ε_c^0	Compressive strain in fibre direction at damage initiation	-0.0125
$G_{Ic}^{f,T}$	Critical energy release rate in mode I for tensile case	100 N/mm
$G_{Ic}^{f,C}$	Critical energy release rate in mode I for compressive case	40 N/mm
Delamination		
G_{Ic}^{del}	Critical energy release rate in opening mode I	0.5 N/mm
G_{IIc}^{del}	Critical energy release rate in shear mode II	1.6 N/mm

Matrix cracking		
σ_t^f	Transverse tensile strength	50 MPa
τ_{lt}^f	In-plane shear strength	90 MPa

3.3. Modelling of specimens and consideration of the wrinkles

The entire specimen was meshed with elements of the same size, generated by an external script. In a first step, a plate was generated and then the positions of the nodes were projected at 45° for the constitutive elements of the arms and on a quarter cylinder for the elements forming the radius of curvature (Fig. 2).

The wrinkles were taken into account by a point statement, which was used to recalculate the position of the nodes corresponding to experimental interfaces previously measured on an image of the specimen side face obtained during experiment. The new node coordinates ensured that all elements were orientated along the axis and passed through the theoretical origin of the radius of curvature.

The modelling of wrinkles may lead to important modifications of the initial elements modelled and the variation of stiffness needs to be considered. On the example of Fig. 4, the modelling of the ply wrinkling has significant influence on the section of the volume element highlighted in red (Fig. 4.b) compared to the same element of the pristine specimen (Fig. 4.a). The section variation leads to a stiffness variation corresponding to a variation of fibre volume ratio. A coefficient, called *CoefS*, was calculated to correspond to the ratio between the initial section and the deformed section (Eq. 4).

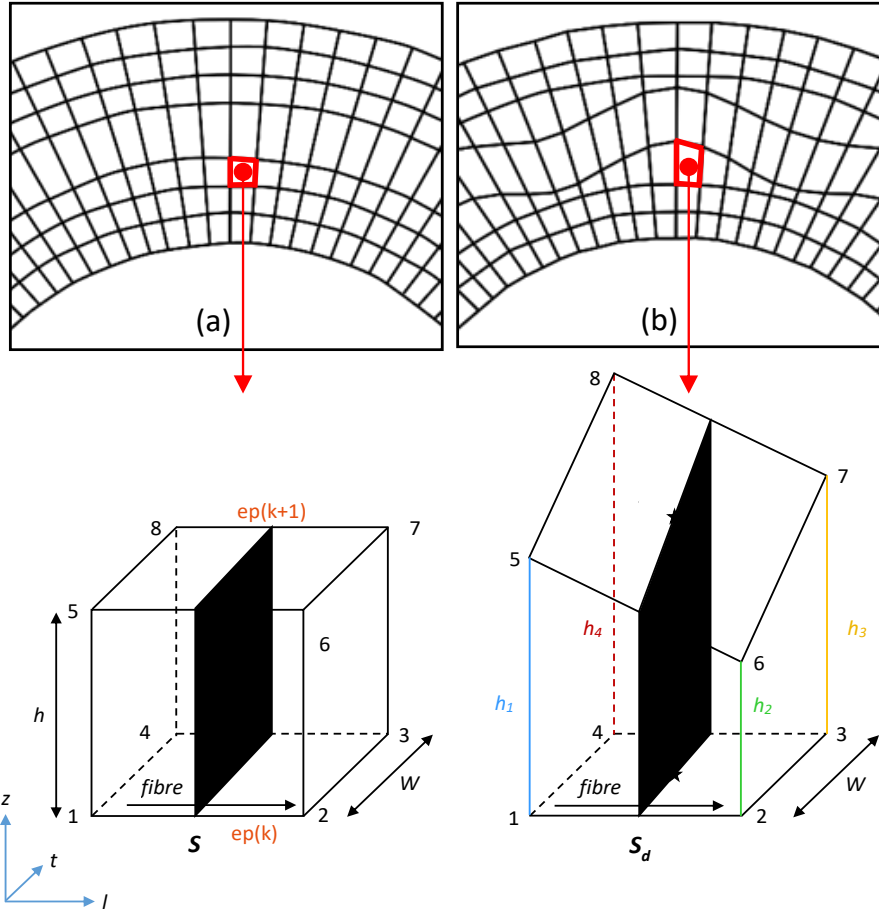


Fig. 4: (a) 2D view of the mesh of a pristine specimen, indicating an initial volume element, (b) 2D view of the mesh of a specimen taking ply wrinkling into consideration, which points out a deformed volume element

$$CoefS = \frac{S_d}{S} \quad (\text{Eq. 4})$$

where S represents the initial section corresponding to the theoretical thickness of the ply and S_d corresponds to the deformed section, which is calculated as the average of the four distances noted h_1 , h_2 , h_3 and h_4 multiplied by the width of the element (perpendicular to the direction of the fibres, which remains constant for all elements) (Fig. 4): $S = Wh$ and $S_d = W \frac{h_1+h_2+h_3+h_4}{4}$. The sections to be considered depend on the fibre directions (0° , 90° and $\pm 45^\circ$) and are summarized in Fig. 5.

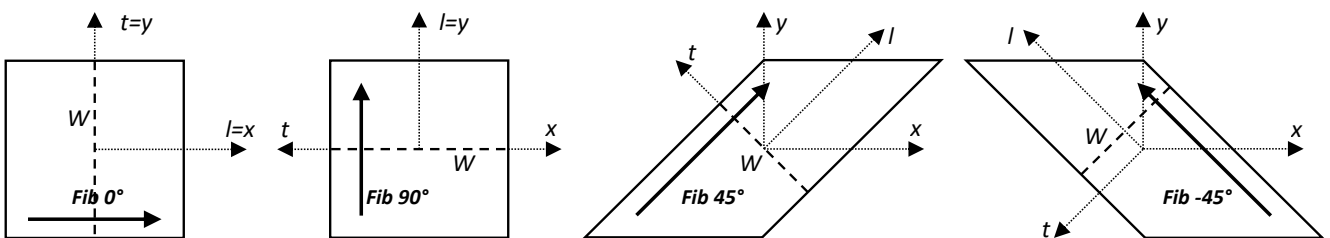


Fig. 5: Representation of sections calculated for each fibre orientation

The construction of the DPM imposed a parallelogram shape for the $\pm 45^\circ$ elements (Fig. 5) to respect the coincidence between the nodes of two stacked plies, as illustrated in Fig. 6 [34–37,39]. The coincidence of four nodes was necessary to allow the coupling between delaminations and matrix cracking. Pairs of nodes (a,b) and (c,d) were used to take the matrix cracking of their own ply into account. The delamination was taken into account by the nodes (a,b) of the upper ply and the nodes (c,d) of the lower ply (Fig. 6).

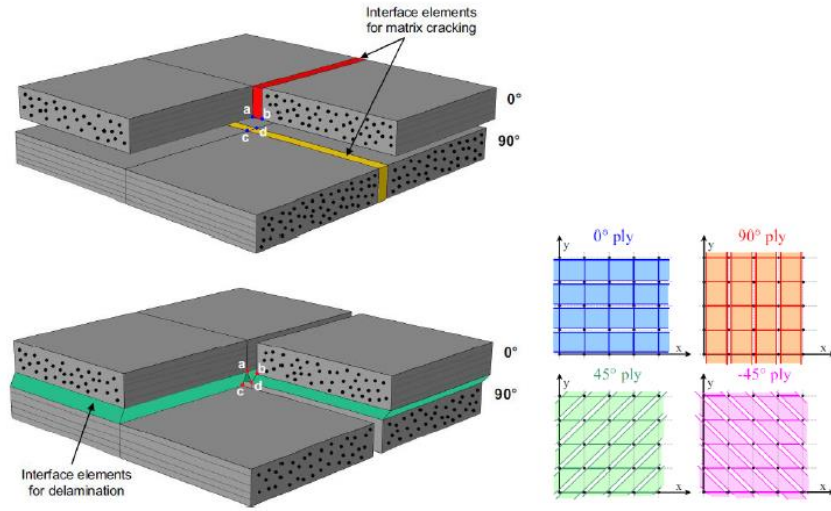


Fig. 6: Coincidence between nodes of two stacked plies [37]

The ratio between the initial and the deformed section was computed for each volume element and the longitudinal modulus (for tensile and compressive cases) was divided by this coefficient in such a way as to respect Eq. 5. Thus, when the section increased, the longitudinal modulus decreased and when the section decreased, the longitudinal modulus increased. Similarly, the critical energy release rate (for tensile and compressive cases) was divided by the same coefficient to dissipate the right amount of energy and to respect Eq. 6.

$$E_l S = E_d S_d, \text{ with } E_d = \frac{E_l}{\text{Coefs}} \quad (\text{Eq. 5})$$

$$G_{IC}^f \cdot S = G_{IC}^{f,d} \cdot S_d, \text{ with } G_{IC}^{f,d} = \frac{G_{IC}^f}{\text{Coefs}} \quad (\text{Eq.6})$$

where E_l is the longitudinal modulus and G_{IC}^f is the critical energy release rate in mode I for tensile or compressive cases (Table 2).

A local coordinate system was calculated and assigned to each element volume to obtain a fibre axis that corresponded to a deformed element as illustrated in Fig. 4. The global coordinate system of the specimen is represented in Fig. 2. The longitudinal vector as calculated by the average between coordinates of nodes (1;2) and (3;4) of the lower surfaces of the elements and coordinates of nodes (5;6) and (7;8) belonging to the upper face (Fig. 4). The out-of-plane vector was calculated by the average of the scalar product between coordinates of nodes (1;3) and (2;4) for the lower surface and coordinates of nodes (5;7) and (6;8) for the upper one (Fig. 4). The transversal vector was calculated by the cross product of the longitudinal and out-of-plane vectors. Then, the orientation of fibres was checked to match the theory. If the geometrical fibre orientation imposed by the position of the nodes differed by more than 0.1° , the fibre orientation was recalculated and reallocated to the volume element. This particularly applied for the $\pm 45^\circ$ elements in the curvature part because the mesh was projected on to the curved part by using a mean radius of curvature. In the example of Fig. 7, the coordinate statement of the deformed element (in red on Fig. 7) was turned by α° to correspond to the theoretical orientation of 45° of the pristine element (in blue) in the (x,y) plane. Therefore, each volume element had its own coordinate system with a mean longitudinal vector. When wrinkles were taken into consideration by the mesh, the coordinate systems of volume elements matched, with their mean orientation and the fibre orientation reflecting reality.

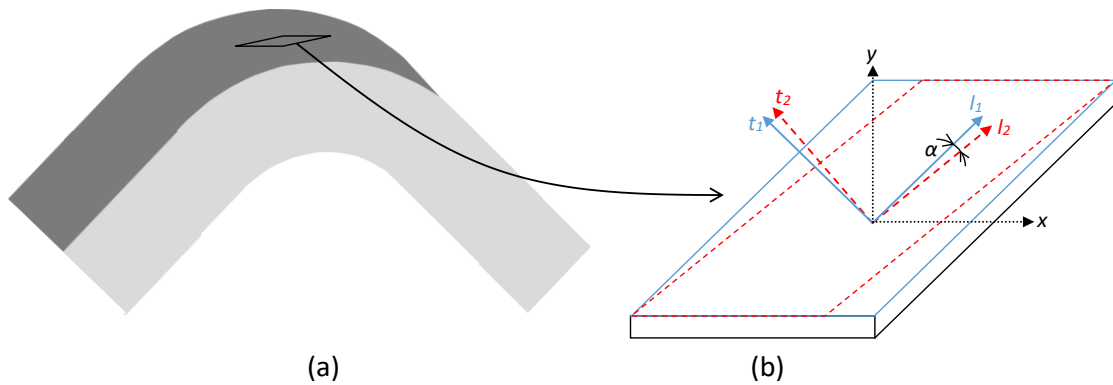


Fig. 7: (a) 3D view of the curved specimen. (b) Case of 45° orientation with, in blue, the non-deformed element and, in red, the element deformed due to the 3D shape of the specimen

4. Numerical modelling of defects on L-angle specimens under four-point bending tests

This part focuses on comparing experimental and numerical simulations of four-point bending tests on L-angle specimens with presence of defects. Two types of defects pointed out in a previous study [31] are modelled and studied here: pre-delamination and wrinkle defects. First, the EM-1_1.5° specimen with

the lower level of wrinkles is considered as a reference here and is modelled and simulated without wrinkles but with presence of pre-delamination defects. In a second part, an EP-1/8_26° specimen with a medium level of wrinkles is modelled and simulated. Then, EP-1/2_66° with wrinkles and pre-delamination defects is modelled and simulated to study the influence of each defect on the failure of the specimen. A comparison is made between experimental and numerical failure load for different initial delamination lengths and misalignment angles. To finish, a numerical discussion of the variation of the failure load in relation with the misalignment angle (with and without initial delamination defect) is proposed.

4.1. Without wrinkles and with pre-delamination defect: EM-1_1.5°

The maximum misalignment angle (noted ϑ_{max}) relative to the reference surface (Fig. 8), corresponding to the external one in the case of the EM-1_1.5° specimen, was measured equal to $1.5 \pm 2^\circ$, which is very low and can be neglected. Therefore, the sample was taken as the reference here and no wrinkles were modelled in this case. The misalignment was measured from experimental data and corresponded to the difference between the maximum misalignment of wrinkle α_1 and the angle of the reference surface α_2 . The maximum misalignment angle ϑ_{max} was measured with a precision of $\pm 2^\circ$. Each side face of the specimen is presented in Fig. 9; one of them shows an initial delamination between two 0° plies but nothing was visible on the other side. This defect measured 2 mm in length.

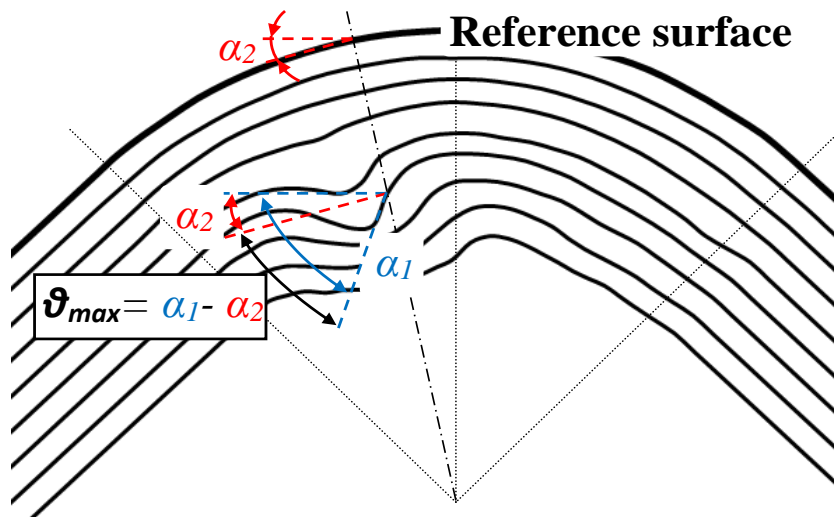


Fig. 8: Measurement of the maximum misalignment angle

The experimental test was instrumented by Digital Image Correlation on one side of the specimen and infrared thermography on the other side. The Load – Machine Displacement curves showed a first load drop at 380 N and 5 mm of machine displacement (Fig. 11). This was driven by the interlaminar fracture

between the $[90_2/0_2]$ layers on the lower part of the specimen and by delamination between 0° plies at the middle of the thickness of the specimen. A second load drop occurred at 370 N and 7.2 mm of displacement and was caused by the propagation of delamination previously initiated at the same interface. Then, a last significant load drop appeared, due to delamination between $[90/-45]$ plies, between $[0/90]$ plies and by matrix cracking of the 90° ply in the upper part of the specimen. Interested readers are invited to refer to [31] for more details on the experimental failure of this specimen.

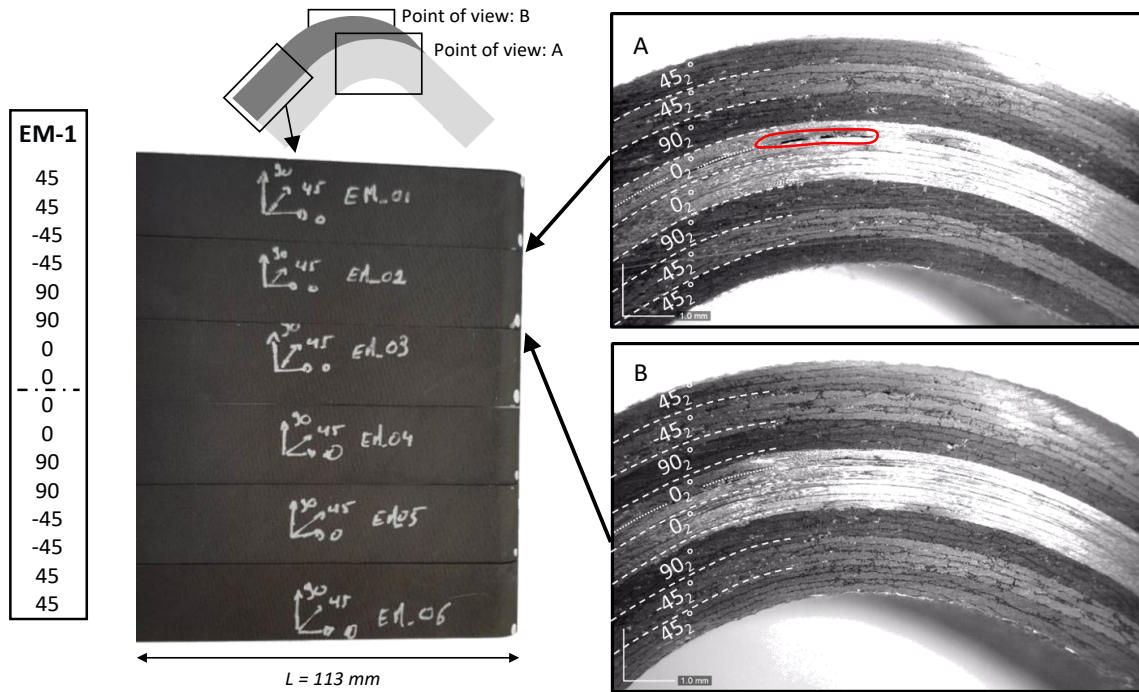


Fig. 9: EM-1_1.5±2° specimen side faces

The proposed numerical model has one volume element in the thickness for two plies of the same orientation, except for the 0° plies around the central one, which have a mesh with a single element in the thickness for the ply (Fig. 10). Thus, interface elements are present at the interface corresponding to the initial delamination highlighted in Fig. 9. Due to the semi-continuous construction of the DPM, it was possible to define a different value of the initial damage internal variable of the interlaminar elements corresponding to the pre-delaminated length observed experimentally. Pre-delaminated length was assumed constant through the width of the specimen. Simulations were run without any damage (to consider the pristine case) and with three different pre-delaminated lengths, noted L_d , (4 mm, 2 mm and 1 mm) to study their influence on the load-machine displacement curves and on the out-of-plane strength.

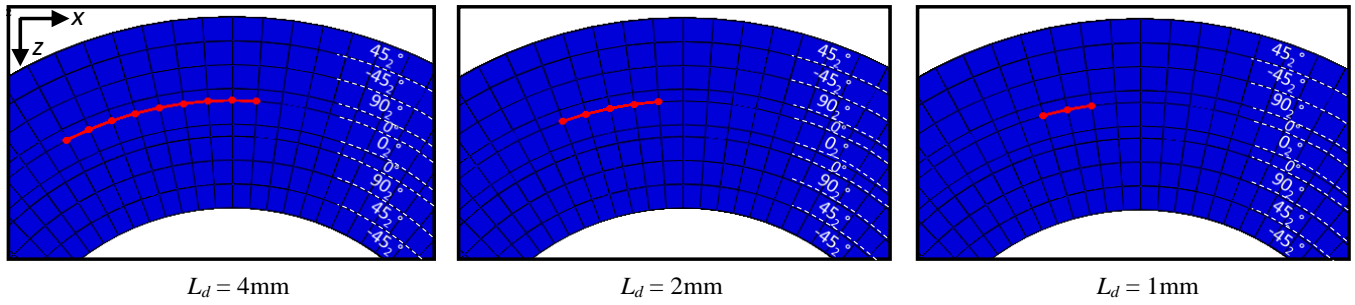


Fig. 10: Three different levels of pre-delaminated lengths

The experimental envelope curve (formed by the maximum and the minimum values of the six experimental Loads and Machine displacements) is presented in light blue on Fig. 11. The other four curves correspond to load-machine displacement curves produced by the DPM. The dark one corresponds to a pristine specimen without pre-damage of any interlaminar elements. The blue ones correspond to the EM-1_1.5° specimen with the three different levels of pre-delaminated lengths. It is clear that pre-damage of some interlaminar elements had a significant effect on the failure load. The pristine sample failed at a load of 650 N whereas the specimen with a pre-delaminated length of 1 mm had a failure load of approximately 460 N, which represents a difference of 190 N for a pre-delaminated area of 20 mm². The simulation with a pre-delaminated length of 2 mm gave a failure load of 350 N and, for the specimen with a pre-delaminated length of 4 mm, the failure load was 290 N. Compared to the mean experimental failure load (400 N) the value of the failure load provided by the simulation with a pre-delaminated length of 2 mm, which was experimentally measured on one of the side faces of the specimen, was the closest. Moreover, the value of the failure load corresponding to this specimen was 380 N, which is clearly consistent with the simulation. It is noteworthy that the stiffness of the numerical load-machine displacement curves matched the experimental one. The model showed a reacting load without a second load drop as experimentally observed due to the propagation of damage through the thickness of the specimen.

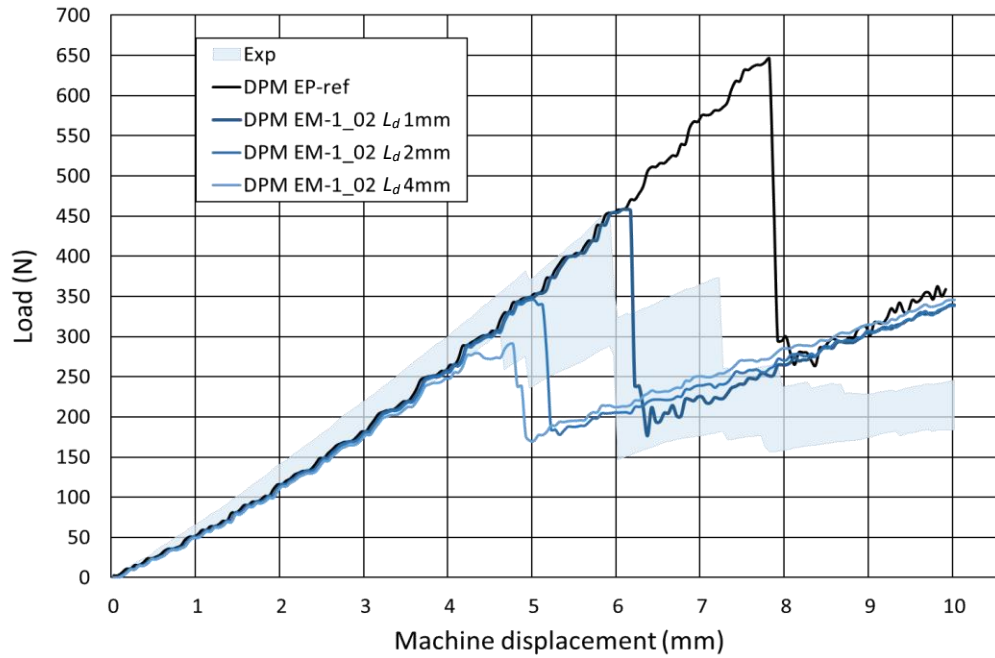
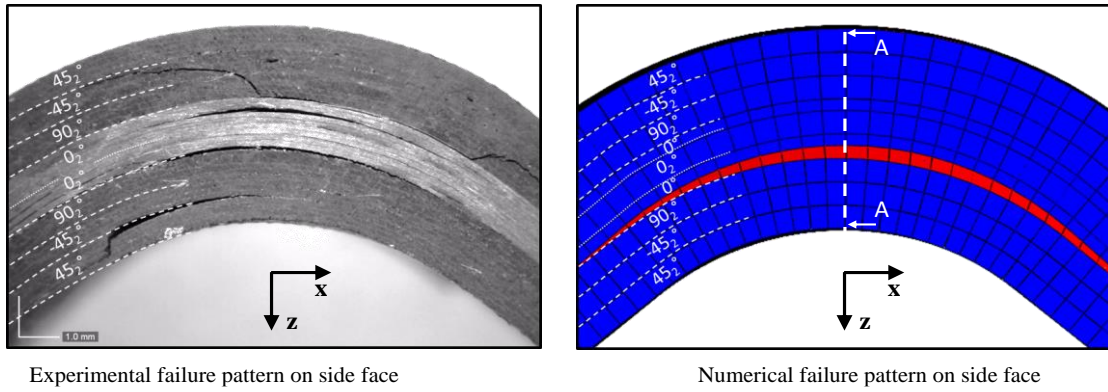


Fig. 11: Load-Machine displacement curves of the EM-1_1.5° specimens

On the numerical curves, the load drops were due to delamination [90/0] in the lower part of the specimen and the propagation of the pre-damaged to the interlaminar elements. That was in agreement with the experimental damage (Fig. 12), which caused the main load drop in the experimental load-machine displacement curves. Delaminations were driven by the out-of-plane tensile stress concentrations (Fig. 13). It should be noted that the numerical results presented on Fig. 13 and Fig. 14 are for the case of the specimen with a pre-delamination of interface elements over a length of 2 mm, which was the most realistic case relative to the experimental investigations. The interlaminar elements of the interface [0/0] were the first to be damaged, followed by the elements composing the interface [90/0] in the lower part of the specimen (Fig. 14). Of course, the energy released by the interfaces [0/0] and [90/0] was mainly dissipated in mode I. In the case of the pristine sample, the [90/0] interface was the first to initiate delamination, followed by the interface [0/0] in the lower part of the specimen and, finally, the [0/0] interface broke in the upper part of the specimen (Fig. 15). This leads us to conclude on the importance of considering the pre-delaminated defect, which drives the initiation of delamination and therefore the failure of the specimen.



Experimental failure pattern on side face

Numerical failure pattern on side face

Fig. 12: Comparison between experiment and numerical failure side face

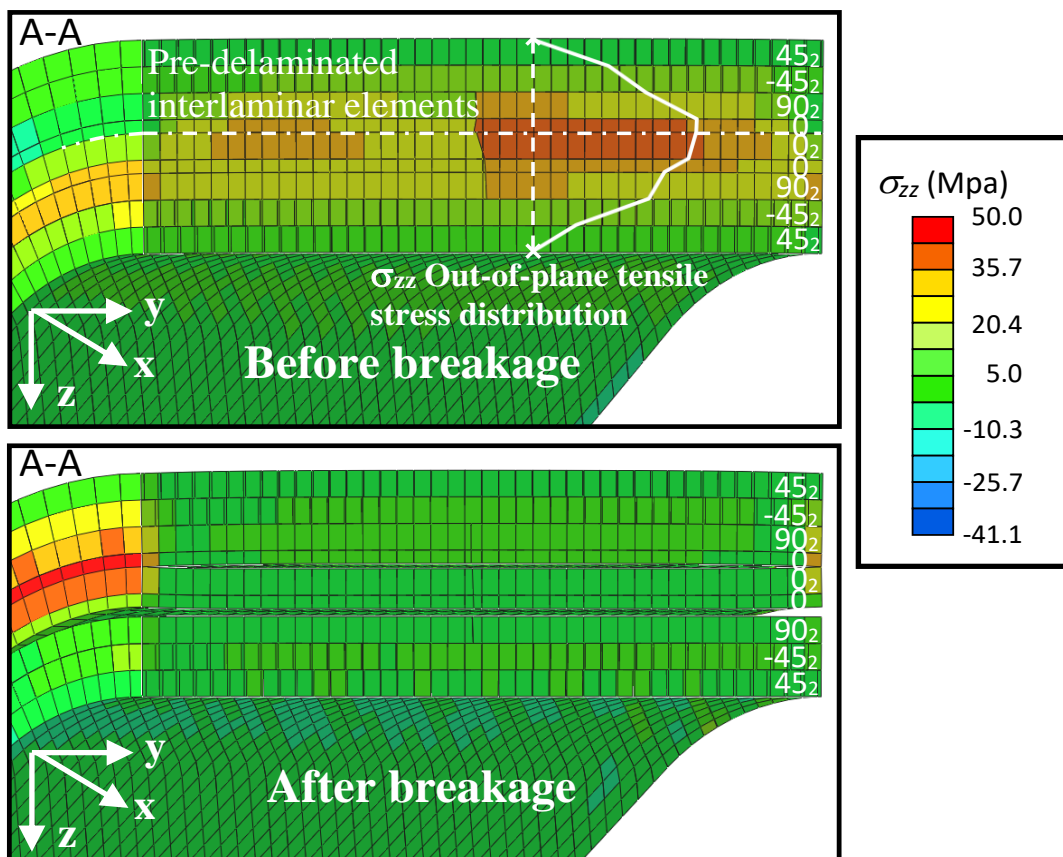


Fig. 13: Stress distribution through the section view A-A (defined on Fig. 12) of the specimen EM-1_1.5° with a pre-delaminated length of 2 mm

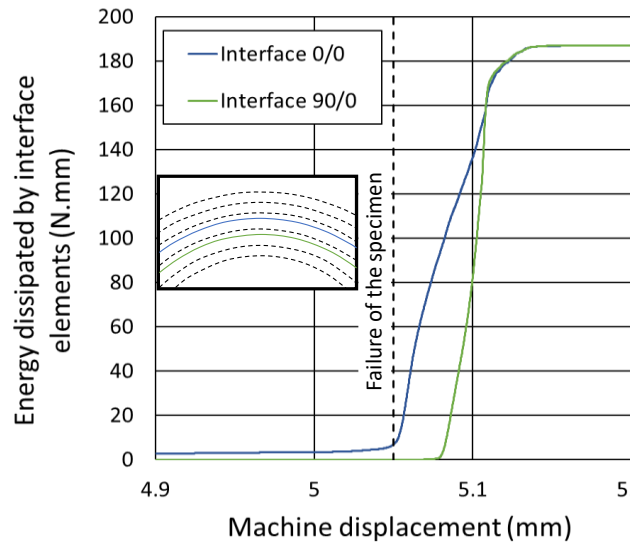


Fig. 14: Energy dissipated by interface elements – EM-1_1.5° specimen with a pre-delaminated length of 2 mm

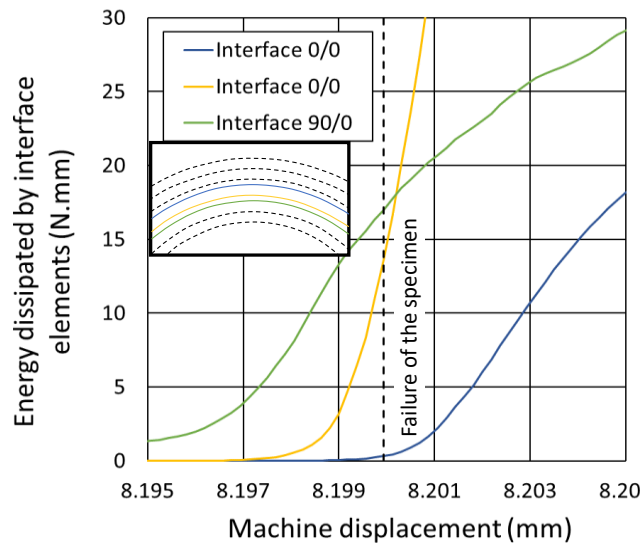


Fig. 15: Energy dissipated by interface elements - pristine specimen

4.2. Intermediate level of wrinkles without pre-delamination defect: EP-1/8_26°

The EP-1/8 batch of specimens were made in a concave mould and the two central plies at 0° were previously laid up by hand on a flat surface before being introduced into the mould. In this way, the mean value of maximum misalignment angle measurements was 26.4° with respect to the reference surface, which corresponds to the surface in contact with the mould, the external one here (Fig. 17). In contrast to

the previous case, no initial delamination can be noted on these two side faces (Fig. 16). Nevertheless, it is worth noting that $[45_2/-45_2/90_2/0_2]$ plies, in the lower part of the specimen, were affected by wrinkles.

An image of the specimen was used to make a point statement of each interface between plies with different orientations. Then, it was used to modify the initial mesh of the specimen and take the wrinkling of some plies into consideration. The model produced by means of the point statement is represented in Fig. 17 and interfaces between plies are plotted in white on the experimental images, which were used for the measurements. This method allows perfectly realistic modelling of the wrinkles. Concerning the specimen studied in this part, the maximum misalignment angle measured relative to the reference surface was 26° and it is localised by a black circle in Fig. 17.

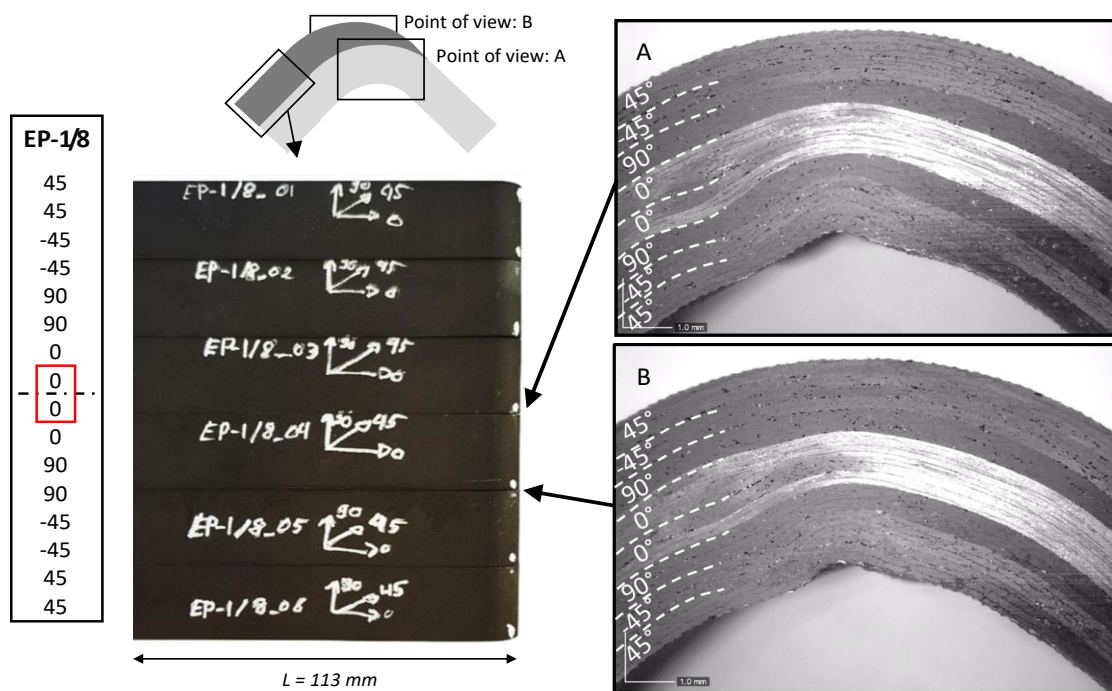


Fig. 16: EP-1/8_26° specimen side faces

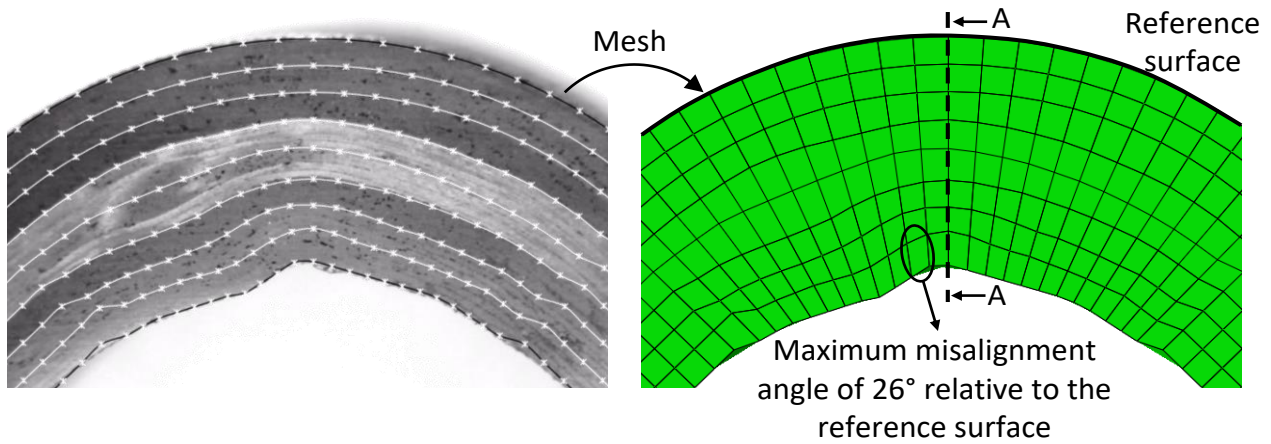


Fig. 17: Comparison between experiment side face and meshed specimen EP-1/8_26°

The experimental envelope of the load-machine displacement curve corresponding to the four-point bending tests conducted on the six specimens of the batch EP-1/8 is plotted on the graph of Fig. 18. The results show low variability regarding the stiffness and the failure load.

The damage scenario is characterised by a first main load drop followed by a succession of smaller load drops due to the propagation of damage through the thickness of the specimen. Interested readers can refer to [31] for more information concerning the damage scenario of this specimen. The load-machine displacement curve corresponding to the simulation of the pristine specimen is plotted in dark blue. The light blue curve corresponds to the numerical model of the EP-1/8_26° specimen, which takes wrinkles into consideration as represented on Fig. 17.

The simulation of the EP-1/8_26° specimen presented a failure load at approximately 400 N, which is 34% higher than the experimental mean failure load. The first load drop was driven by the delamination of the interfaces: [0/0], [90/0] and [-45/90] in the lower part of the specimen (Fig. 19) and matrix cracking of the 90° ply. This was due to out-of-plane tensile stress concentration around these plies in the middle of the specimen (Fig. 20). The stress concentration was maximal at the interface [-45/90] exactly as shown by the DIC on the experimental test of this specimen [31]. These damage occurrences were in agreement with the experimental ones reported on Fig. 19. The second load drop appeared at 290 N and 7.5 mm of machine displacement. It was due to the propagation of damage into the upper part of the specimen and, more particularly, to the delamination of the [90/-45] and [0/90] interfaces (Fig. 20). Matrix cracking was also present into the -45° and 90° plies, consistently with the experimental damage composed of matrix cracking in the 90° ply and delamination of the [90/-45] and [0/90] interfaces (Fig. 19).

Simulation considered only the wrinkling of the plies, which produced a failure load higher than expected, seeing the experimental results. Section 4.1 showed that initial delamination defects have a huge

impact on the simulation in light of the pre-damaged area. In this case, no initial delaminations were visible on the specimen but internal initial delamination defects, porosity or other types of defects may have been present.

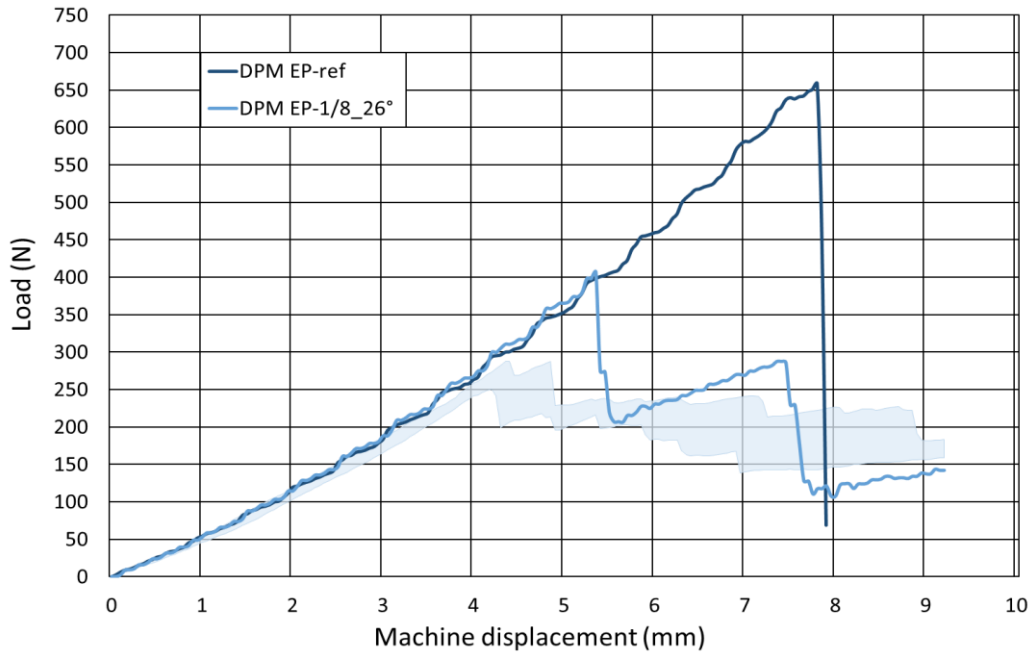


Fig. 18: Load-Machine displacement curves of the EP-1/8_26° specimen

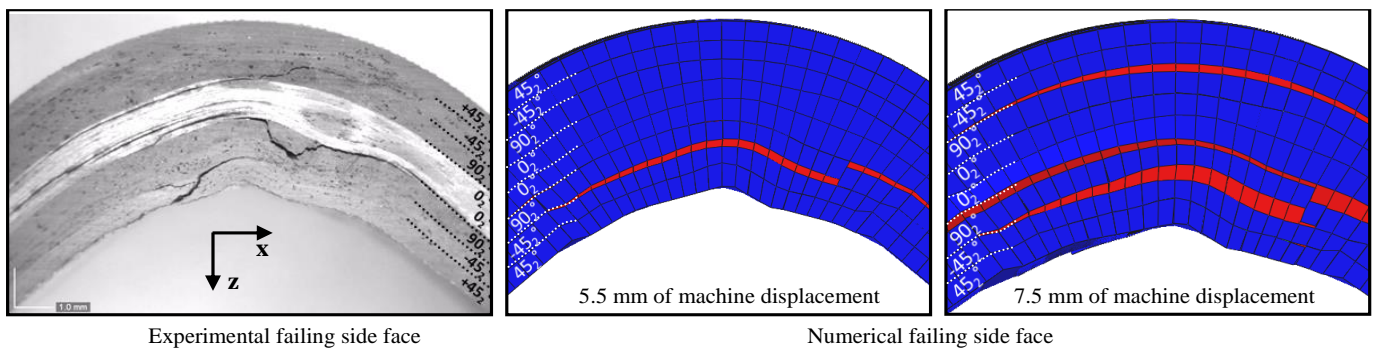


Fig. 19: Comparison between experiment and numerical failure, side face

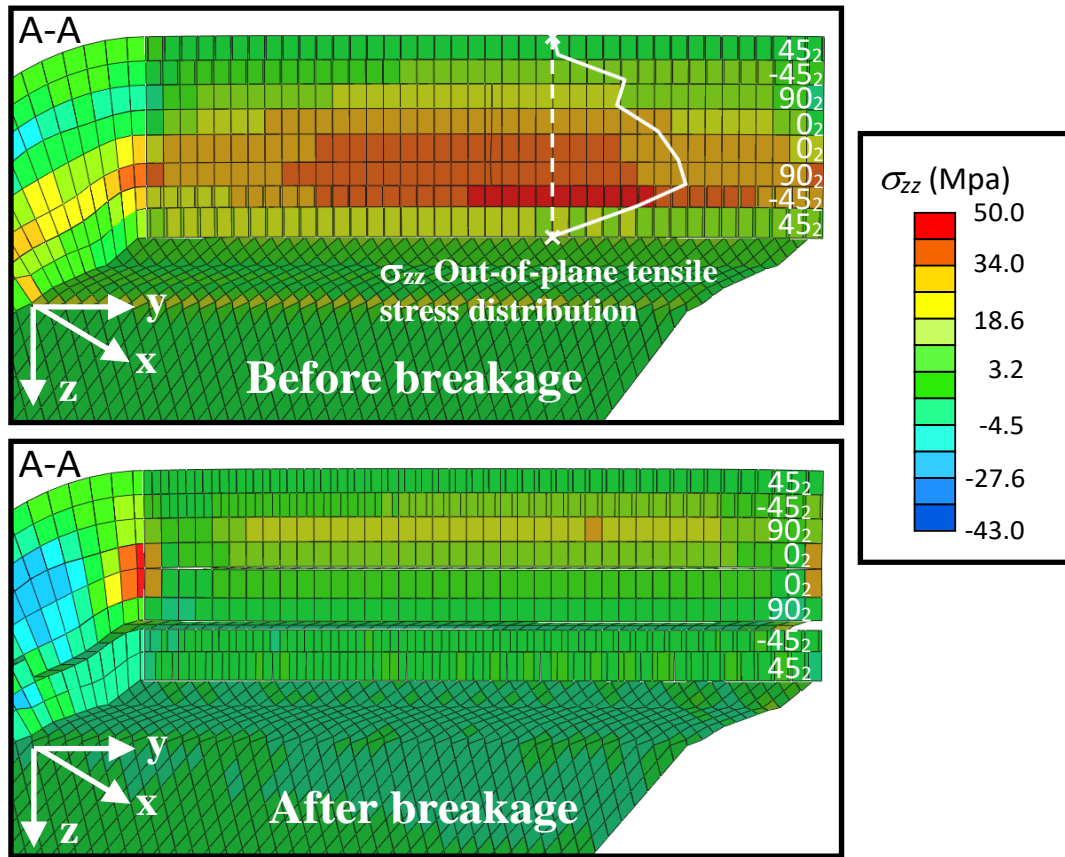


Fig. 20: Stress through the section view A-A (defined in Fig. 17 Fig. 10) of the specimen EP-1/8_26°

4.3. High level of wrinkles and pre-delamination defects: EP-1/2_66°

We recall that this specimen was laid up by hand, using two strategies. First of all, the $[-45_2/45_2]$ plies were directly dropped into the concave mould. Secondly, the $[90_2/0_2/0_2/90_2]$ plies were stacked on a flat surface before being introduced into the concave mould. To conclude, the last $[-45_2/45_2]$ plies were dropped directly into the mould like the first ones. To avoid porosities, pressure was applied with a vacuum bag for fifteen minutes every two plies to ensure good compaction.

Fig. 21 shows the two side faces of the EP-1/2_66° specimen. Porosities located at the interface between two plies caused problems of pre-delamination. These two side faces were very similar in terms of wrinkles but the porosity positions varied slightly. The first picture was chosen to make the point statement used to mesh the part. Fig. 23 presents a comparison between the experiment side and the numerical one. Numerical interlaminar interfaces are plotted in white on the experimental side face to enable the reader to compare them. The location of the maximum misalignment angle, 66° here, was pointed on the numerical side face. This angle was relative to the reference surface, which corresponds to the surface

in contact with the mould. In this case, the reference surface was deformed with respect to the mould geometry. The presence of several wrinkles probably induced additional thermal stresses, which led to a deformed composite laminate after cooling.

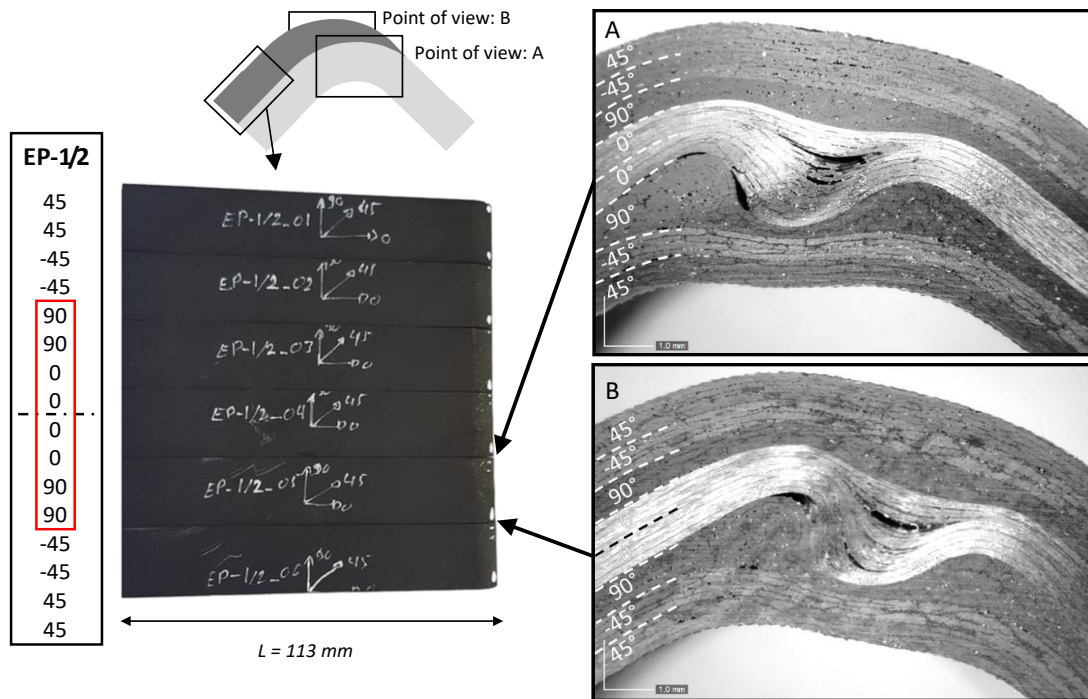


Fig. 21: EP-1/2_66° specimen side faces

The experimental breaking of the EP-1/2_66° specimen was abrupt, with major damage located in the lower region of the part. It was composed of delamination between [90/0] and [-45/90] plies and matrix cracking of the 90° ply. Moreover, delamination between [45/-45] plies in the lower part of the specimen, between [0/90] plies in the upper part of the specimen, and matrix cracking of the 90° ply, were also present. Digital Image Correlation (DIC) confirms that wrinkles induced out-of-plane tensile strain concentration (Fig. 22). An infrared thermography camera showed that the main damage was located around [-45/90/0] plies in the lower part of the specimen (Fig. 22).

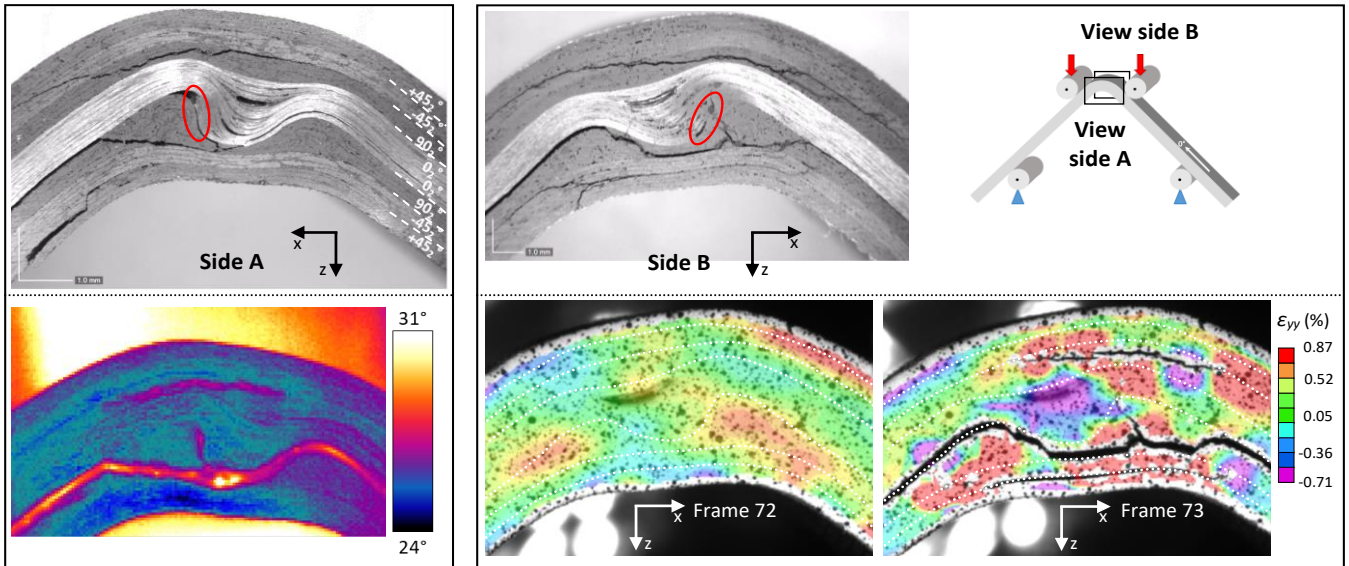


Fig. 22: Damage scenario of the EP-1/2_66° specimen. In the upper part of the figure, the failed section of sides A and B. On the left of the figure, infrared thermography images and, on the right of the figure, the DIC.

Given the results presented in Section 4.1, it was decided to take initial delamination problems into consideration. Interlaminar interface elements, corresponding to the pre-delaminated area highlighted in red in Fig. 23, were pre-damaged using the damage variable with an initial value of 1 on a total length of $L_d = 3.8$ mm. The pre-damaged area was assumed to be constant through the width of the specimen as well as the wrinkles.

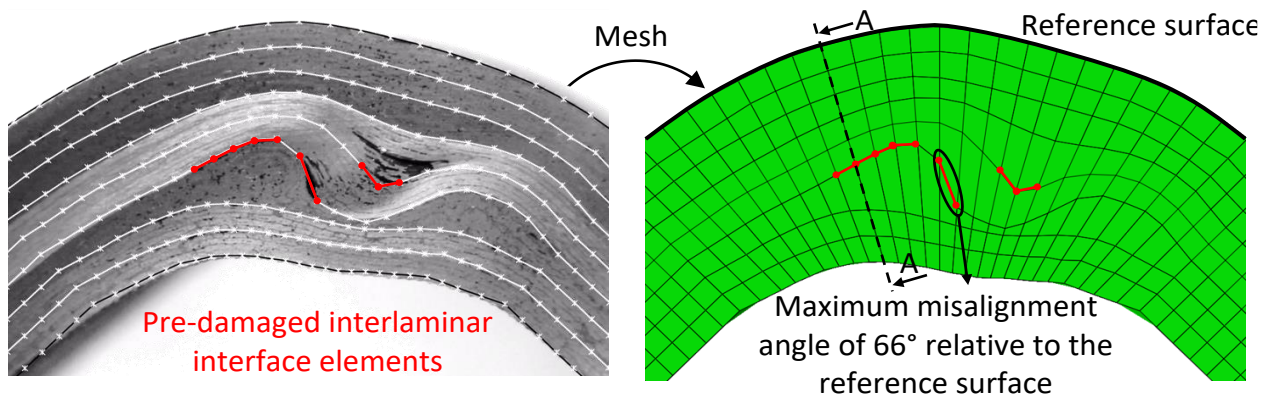


Fig. 23: Comparison between experimental side face and meshed specimen

The experimental Load-Machine displacement envelope curve corresponding to the four-point bending tests conducted on six specimens of the batch is plotted in light blue on Fig. 24. The stiffness of this batch of specimens presents lower variability than the previous batch (EM-1). The numerical simulation of a four-point bending test on a pristine specimen (without wrinkles or initial delamination) is plotted in black. A first simulation with the mesh taking wrinkles into consideration was run and the curve is plotted in dark blue on the graph. The failure load was very similar to that of the simulation on the pristine specimen. Nevertheless, for machine displacement higher than 2 mm, the wrinkles have a slight effect on the stiffness of the specimen (Fig. 24). The last curve, in light blue, corresponds to the model taking wrinkles into consideration and with the pre-delamination of some interlaminar interface elements (in red on Fig. 23). The failure load was 33% lower than the simulation considering only the wrinkle and the stiffness was exactly the same.

The numerical failure load was 15% higher than the mean experimental failure load. The curve presents a main load drop at 422 N and 5.4 mm of machine displacement, which corresponds to delamination of the [90/0] interface (Fig. 26) due to an out-of-plane tensile stress concentration around the 90° ply in the lower part of the specimen, as visible on the section view A-A of Fig. 25. The matrix cracking of the 90° ply within the lower part of the specimen was also damage. Moreover, pre-damaged interlaminar interface elements constitutive of the [0/0] interface spread through the interface. Then the [90/-45] interface was damaged in the upper part of the specimen, located just above the pre-damaged elements of the [0/0]. This was perfectly in agreement with the experimental observations (Fig. 22).

A second load drop was visible around 7 mm on the load-machine displacement curve. This was due to propagation of initial delaminations and to the delamination of the [90/-45] interface plies in the upper part of the specimen. This delamination continues to propagate until 8.5 mm of displacement is reached, as shown on Fig. 26. This was in harmony with the damage scenarios of L-angle specimens with presence of wrinkle defects [31], which were characterised by first damage located in the lower part of the specimen around the 90° ply followed by delaminations and matrix cracking of the -45° and 90° plies located above the 0° plies.

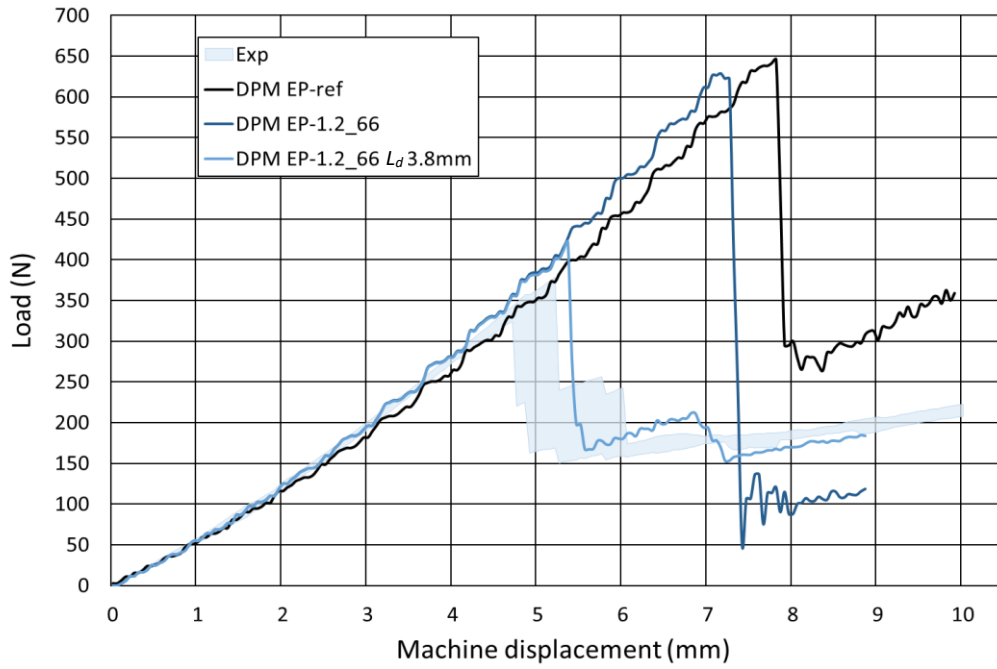


Fig. 24: Load-Machine displacement curves of the EP-1-2_66° specimen

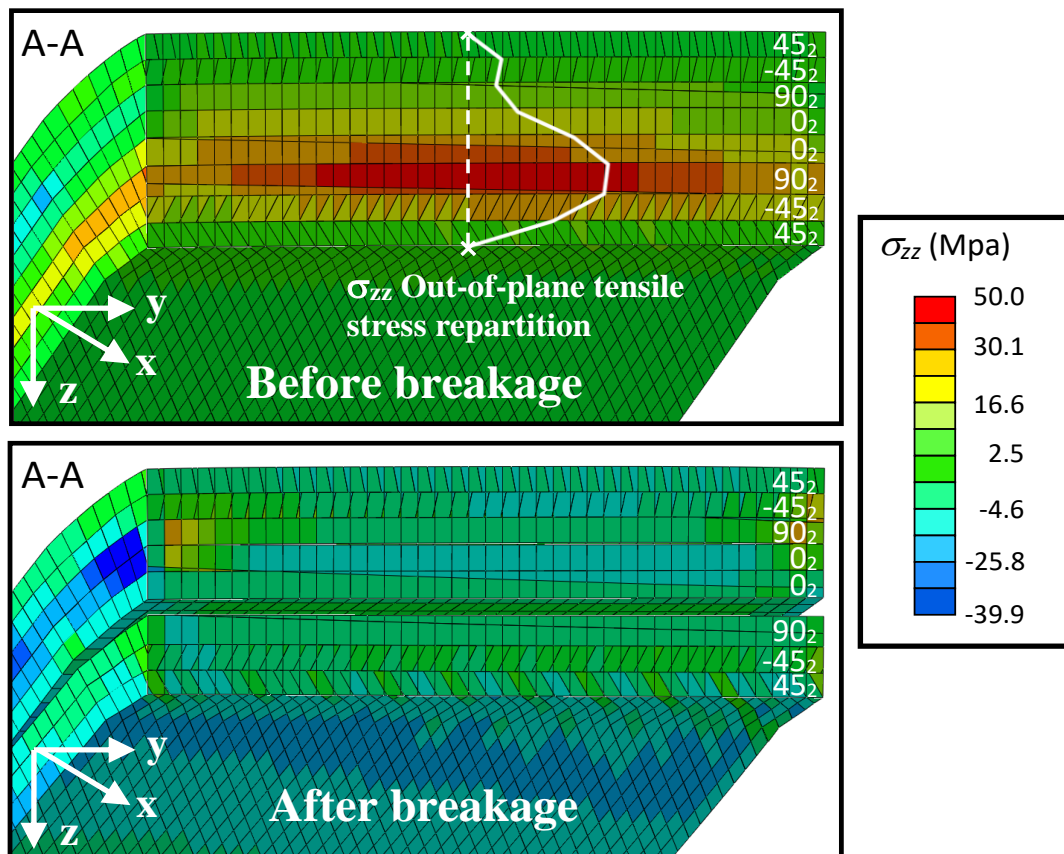


Fig. 25: Stress distribution through the section view A-A (defined on Fig. 23) of the EP-1/2_66° specimen

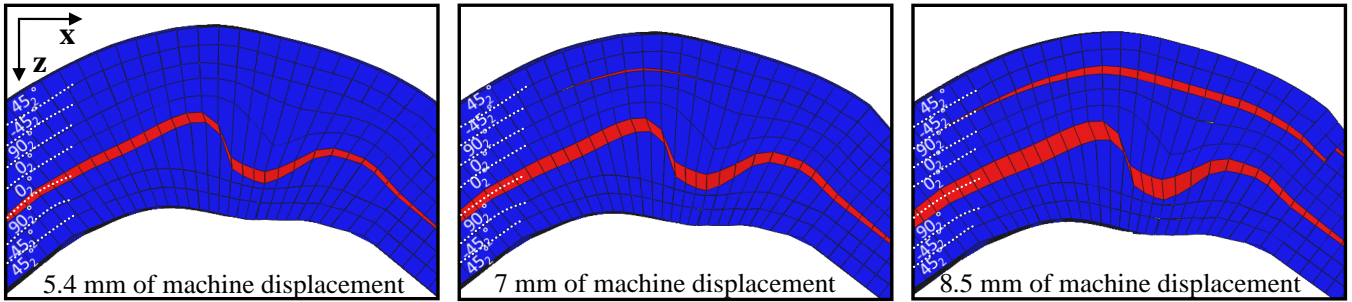
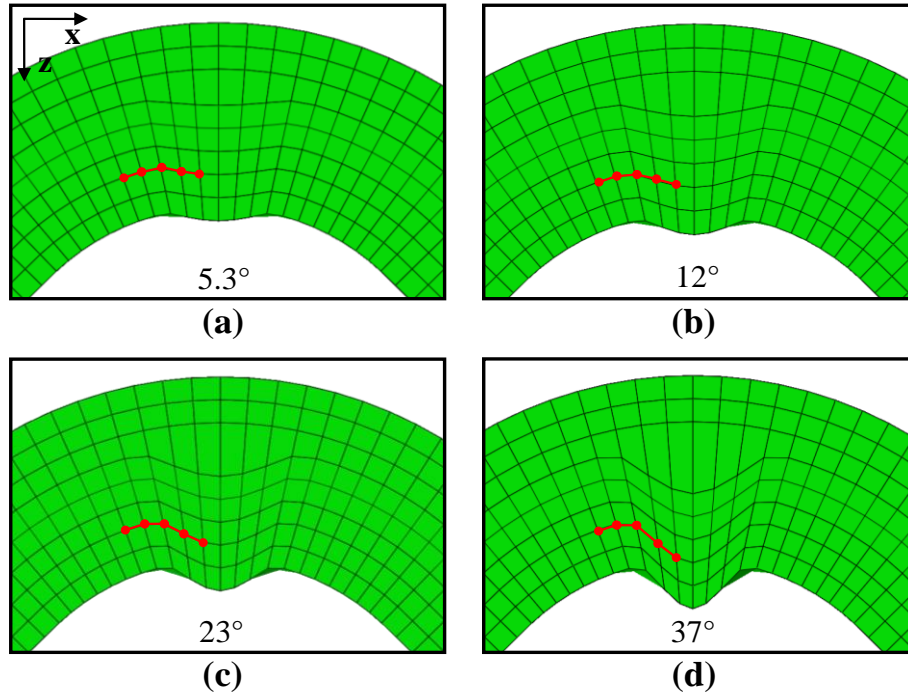


Fig. 26: Numerical damage for three levels of machine displacement

4.4. Numerical discussion of the variation of the failure load in relation with the misalignment angle (with and without initial delamination defect)

In this section, four theoretical levels of wrinkles were introduced and modelled by a cosine function. The four wrinkle levels are presented in Fig. 27, where specimen (a) had a maximum misalignment angle of 5.3° , specimen (b) 12° , specimen (c) 23° and specimen (d) 37° of maximum misalignment angle relative to the reference surface, which corresponded to the outer radius here. Simulations were run on these four specimens without initial delamination defects. Then initial delamination was introduced in each specimen to study the combined influence of initial delamination and wrinkle defects. Pre-damaged interface elements are highlighted in red on Fig. 27 and the length of pre-damaged elements, L_d , was chosen to be approximately 2 mm (1.8 mm for specimen (a) and 2.0 mm for specimen (d)), which correspond to the length measured experimentally on specimen EM-1_1.5°.



Pre-damaged interlaminar interface elements

Fig. 27: Sections of the four wrinkle levels studied with, in red, the localisation of pre-damaged interlaminar interface elements. (a) 5.3° of misalignment, (b) 12° of misalignment, (c) 23° of misalignment and (d) 37° of misalignment.

Numerical results are plotted on Fig. 28, which presents the failure loads of the four specimens without initial delamination defects in blue and, in red, the failure load of the four specimens with initial delamination defects taken into consideration. The increase of the misalignment angle has the logical effect of reducing the failure load. As highlighted in Section 4.1, increasing the length of pre-damaged interface elements tended to decrease the resulting failure load. The presence of initial delamination tended to reduce the failure load compared to cases without initial delamination defects. Nevertheless, it should be noted that, for a fixed length of pre-damaged interlaminar interface elements equal to $L_d = 2$ mm, increasing the misalignment angle had no effect on the value of the failure load up to 12° of misalignment angle. After this point, the failure load tended to increase with the misalignment angle. At the maximum of misalignment angle, $\vartheta_{max} = 37^\circ$, the difference of failure loads between simulations of specimens with and without initial delamination defects was very small.

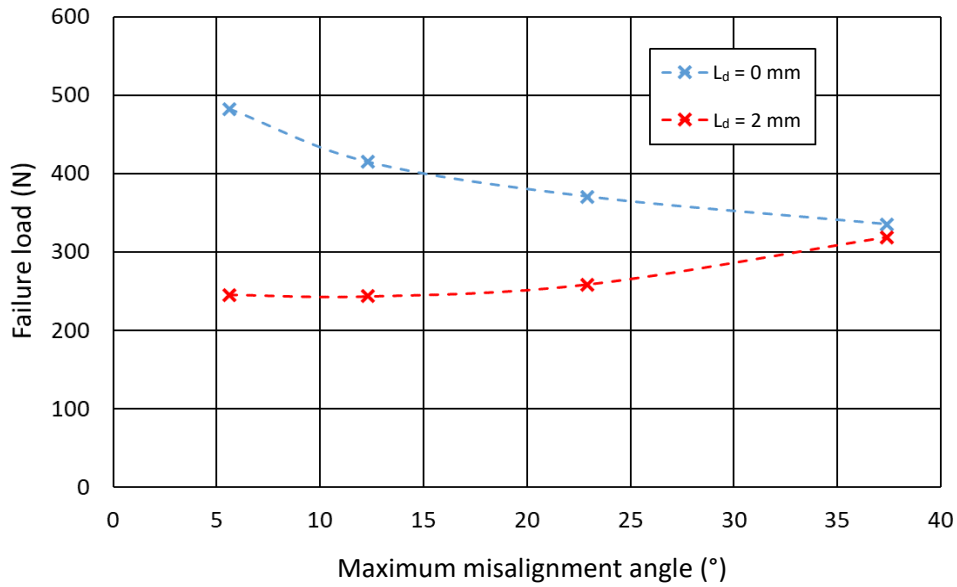


Fig. 28: Variation of the failure loads in relation to pre-damaged length equal to $L_d = 2$ mm in red and without initial delamination in blue for different misalignment angle

4.5. Comparison between experimental and numerical failure loads for various levels of misalignment and initial delamination length

This section presents a comparison between the experimental and the numerical distributions of the failure loads according to the maximum misalignment angles (Fig. 29). Forty-two L-angle specimens, divided into seven batches, were manufactured and tested under four-point bending. Maximum misalignment angles were measured between $1.5 \pm 2^\circ$ and $83 \pm 2^\circ$. Their failure loads are represented by a black dots on Fig. 29. Failure loads estimated from simulations studied previously are symbolised by red crosses on Fig. 29. This graph largely represents the influence of initial delamination on the failure loads of L-angle samples without any wrinkle defects (in the case of EM-1 batch). Specimens with wrinkle defects are correctly represented. However, EP-1/8_26° specimens did not present any visible initial delamination defects but, in the light of the difference between experimental and numerical estimated failure loads, it seems that they could have been subject to internal initial delamination defects. Model results were conservative in comparison with experimental results. Nevertheless, they enabled the effect of wrinkles and initial delamination defects on the failure loads to be studied independently. Some damage may have been missed by the model due to lack of knowledge of embedded defects. In regard to these results, non-destructive testing, such as C-scans or tomography, would have been needed to characterise initial delamination defects.

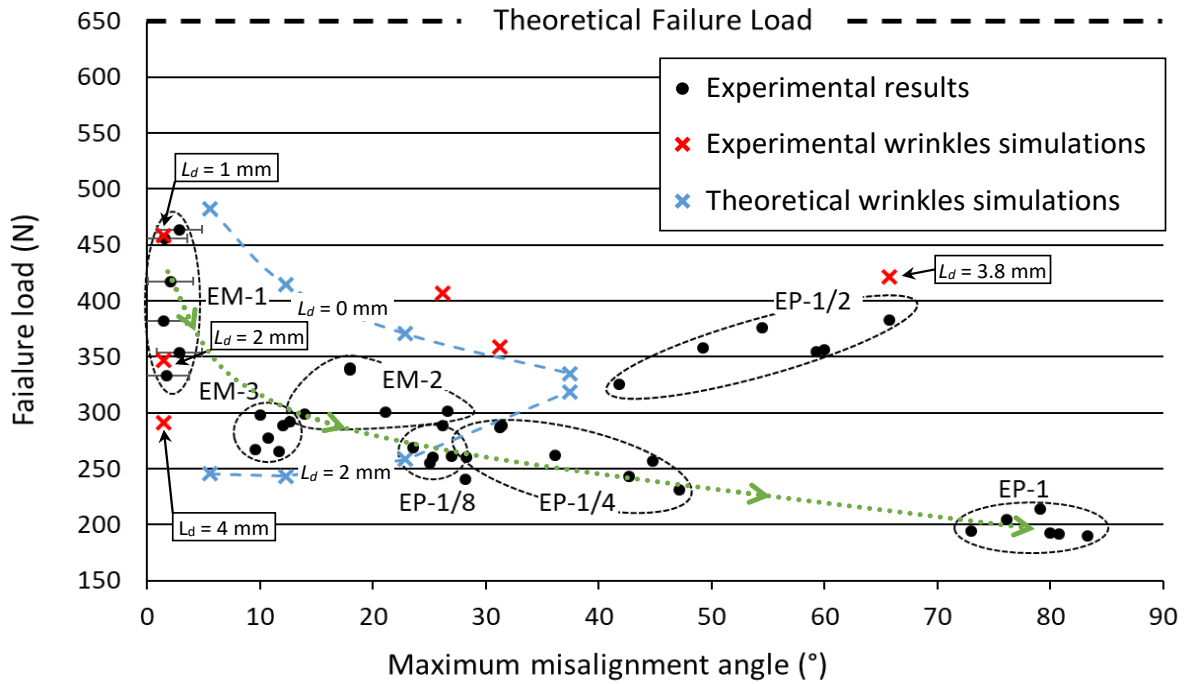


Fig. 29: Distribution of failure loads according to the maximum misalignment angle and pre-delaminated length for experimental and numerical results

5. Conclusions

Based on experimental observations, a numerical model has been developed to take wrinkle defects into consideration on L-angle specimens under four-point bending tests. The Discrete Ply Model (DPM) used in this study has already been used to model four-point bending tests on L-angle specimens without defects [22]. The load-machine displacement curves were representative of the experimental ones. The model gives a load-machine displacement curve and damage pattern that is highly representative of experiments. It predicts maximal load, different load drops and different reaction loads in good agreement for the four stacking sequences studied. This first study gives us confidence in the simulation produced by the DPM and that bodes well for the four-point bending tests on L-angle specimens with presence of defects.

Two types of defects have been studied in this paper, wrinkling of plies and initial delamination defects. Section 4.1 focused on a specimen without wrinkle defects but which clearly presented pre-delaminated areas through the width of the specimen. Thanks to the construction of the DPM (Fig. 3), it was possible to initially damage the internal variables of the interlaminar elements corresponding to the pre-delaminated length observed experimentally. In this way, the influence of pre-delaminated length,

considered constant through the width of the L-angle sample and so equivalent to a pre-delaminated area, could be studied. Simulations with three pre-delaminated lengths (1 mm, 2 mm and 4 mm) were run. Failure loads were respectively 458 N, 357 N, 291 N and 650 N for pristine specimens without pre-damaged interface elements. Initial delamination defects had a significant influence on the failure load. Increasing the length of pre-damaged interlaminar interface elements result in a decreased failure load. The load-machine displacement curve corresponding to the model with a pre-delaminated length of 2 mm, as measured on the experimental specimen, was the most representative with respect to the experimental envelope curve. This confirms the necessity to take initial delamination defects on L-angle specimens into consideration for four-point bending tests.

Section 4.2 presented a specimen with no visible initial delamination defect but with wrinkle defects. This specimen was characterised by a maximum misalignment angle of 26° with respect to the reference surface, which corresponds to the mould (external) contact surface. The wrinkles were taken into consideration by a point statement, which was used to fit the mesh at the experimental measurement. The four-point bending test was run on this specimen using the DPM. The load-machine displacement curve showed the same stiffness as with the pristine specimen but the failure load was dramatically affected by the presence of wrinkle defects, changing from 650 N to 406 N. Wrinkling regions induced an out-of-plane tensile stress concentration, which led to the failure of the specimen due to delaminations in its lower part. The failure loads provided by the DPM for the specimens modelled with wrinkles were 34% higher than the experimental mean value. This suggested that core initial delamination defects might be present through the width of this L-angle specimen. Nevertheless, it must be noted that simulations allow two load drops to be distinguished: the first one caused by damage in the lower part of the specimen and the second by damage located in the upper part of the specimen, which was in agreement with the experiments [31].

The third section (4.3) focused on EP-1/2_{66°} specimens, which presented initial delamination defects at some interfaces and a high level of wrinkles (Fig. 23). The maximum misalignment angle was around 66° . In this case, the wrinkle defects did not affect the failure load and only slightly affected the stiffness. When the initial delamination defects were taken into consideration in the model, the failure load dropped drastically, by 200 N. The failure loads were in line with the experimental one in this case and numerical damage was consistent with the damage observed experimentally.

In conclusion, the Discrete Ply Model allows initial delamination defects and wrinkle defects to be modelled. Simulations provide an acceptable correlation between experimental and numerical four-point bending tests on L-angle specimens with defects (Fig. 29). Nevertheless, both of them need to be taken into consideration. Wrinkle defects are correctly estimated from experimental observations but this is not the

case for initial delamination defects. Non-destructive testing such as C-scans or tomography, needs to be used to evaluate pre-delaminated areas in the curvature part of the specimen more precisely before testing. The DPM could be used to simulate experimentally observed defects and qualify or disqualify the part. It distinguishes the influence of different types of defects independently as initial delaminations and wrinkle defects (Fig. 28). It also makes it possible to evaluate the coupling between initial delaminations and wrinkle defects and evaluate the knockdown factor for the evolution of each of them (Fig. 29). In conclusion, the localisation of wrinkle and initial delamination defects could have a major impact on the unfolding failure of curved specimens. It seems important to remember that, although the knockdown factors are important, these results could logically be expected due to the localisation of defects in the radius of the curvature of the curved specimen. Moreover, under four point-bending tests, induced stresses occur through the thickness, which explains their important influence on the failure load of curved specimens with defects. This model can be used to study different types of defects, even for flat parts, and to distinguish the most harmful.

References

- [1] Neveu F, Castanié B, Olivier P. The GAP methodology: A new way to design composite structures. *Mater Des* 2019;172:107755. doi:10.1016/j.matdes.2019.107755.
- [2] O'Brien TK. Characterization of delamination onset and growth in a composite laminate, 1981.
- [3] Wisnom MR. The role of delamination in failure of fibre-reinforced composites. *Philos Trans R Soc A Math Phys Eng Sci* 2012;370:1850–70. doi:10.1098/rsta.2011.0441.
- [4] Paul PC, Saff CR, Sanger KB, Mahler MA, Kan HP, Kautz EF. Out of plane analysis for composite structures. NASA Tech Report, NASA Langley Res Center, Eighth DOD(NASA)FAA Conf Fibrous Compos Struct Des Part 1; p 263-279 1995:263–79.
- [5] Kedward KT, Wilson RS, McLean SK. Flexure of simply curved composite shapes. *Composites* 1989;20:527–36. doi:10.1016/0010-4361(89)90911-7.
- [6] Gözlüklü B, Coker D. Modeling of the dynamic delamination of L-shaped unidirectional laminated composites. *Compos Struct* 2012;94:1430–42. doi:10.1016/j.compstruct.2011.11.015.
- [7] Olsson R. A survey of test methods for multiaxial and out-of-plane strength of composite laminates. *Compos Sci Technol* 2011;71:773–83. doi:10.1016/j.compscitech.2011.01.022.
- [8] Jackson WC, Ifju PG. Through-the-Thickness Tensile Strength of Textile Composites. *Compos*

Mater Test Des 1996;12:218–38. doi:10.1520/stp16547s.

- [9] Jackson WC, Martin RH. An Interlaminar Tensile Strength Specimen. *Compos Mater Test Des* 1993;11:333–54. doi:10.1520/stp12638s.
- [10] Wisnom MR, Atkinson JW. Compressive failure shear instability waviness: experimental investigation of waviness and correlation with analysis. *J Reinf Plast Compos* 1996;15:420–39.
- [11] Kim T, Fletcher TA, Dodwell TJ, Butler R, Scheichl R, Ankersen J, et al. The effect of free edges on inter-laminar performance of curved laminates. *AIAA/ASCE/AHS/ASC, Structures; Struct. Dyn. Mater. Conf.*, 2015, p. 1. doi:10.2514/6.2015-0968.
- [12] Fletcher TA, Kim T, Dodwell TJ, Butler R, Scheichl R, Newley R. Resin treatment of free edges to aid certification of through thickness laminate strength. *Compos Struct* 2016;146:26–33. doi:10.1016/j.compstruct.2016.02.074.
- [13] Sun CT, Kelly SR. Failure in Composite Angle Structures Part I: Initial Failure. *J Reinf Plast Compos* 1988;7:220–32. doi:10.1177/073168448800700302.
- [14] Sun CT, Kelly SR. Failure in Composite Angle Structures Part II: Onset of Delamination. *J Reinf Plast Compos* 1988;7:233–44. doi:10.1177/073168448800700302.
- [15] Huchette C, Vandellos T, Laurin F. *Damage Growth in Aerospace Composites*. Springer; 2015. doi:10.1007/978-3-319-04004-2.
- [16] González-Cantero JM, Graciani E, López-Romano B, París F. Competing mechanisms in the unfolding failure in composite laminates. *Compos Sci Technol* 2018;156:223–30. doi:10.1016/j.compscitech.2017.12.022.
- [17] Hao W, Ge D, Ma Y, Yao X, Shi Y. Experimental investigation on deformation and strength of carbon/epoxy laminated curved beams. *Polym Test* 2012;31:520–6. doi:10.1016/j.polymertesting.2012.02.003.
- [18] Charrier JS, Laurin F, Carrère N, Mahdi S. Determination of the out-of-plane tensile strength using four-point bending tests on laminated L-angle specimens with different stacking sequences and total thicknesses. *Compos Part A Appl Sci Manuf* 2016;81:243–53. doi:10.1016/j.compositesa.2015.11.018.
- [19] Nguyen KH, Ju HW, Truong VH, Kweon JH. Delamination analysis of multi-angle composite curved beams using an out-of-autoclave material. *Compos Struct* 2018;183:320–30.

doi:10.1016/j.compstruct.2017.03.078.

- [20] Cao D, Duan Q, Hu H, Zhong Y, Li S. Computational investigation of both intra-laminar matrix cracking and inter-laminar delamination of curved composite components with cohesive elements. *Compos Struct* 2018;192:300–9. doi:10.1016/j.compstruct.2018.02.072.
- [21] Cao D, Hu H, Duan Q, Song P, Li S. Experimental and three-dimensional numerical investigation of matrix cracking and delamination interaction with edge effect of curved composite laminates. *Compos Struct* 2019;225:111154. doi:10.1016/j.compstruct.2019.111154.
- [22] Journoud P, Bouvet C, Castanié B, Laurin F, Ratsifandrihana L. Experimental and numerical analysis of unfolding failure of L-shaped CFRP specimens. *Compos Struct* 2020;232:111563. doi:10.1016/j.compstruct.2019.111563.
- [23] Andraju LB, Raju G. Continuum and cohesive zone damage models to study intra/inter-laminar failure of curved composite laminates under four-point bending. *Compos Struct* 2020;253:112768. doi:10.1016/j.compstruct.2020.112768.
- [24] Hassan MH, Othman AR, Kamaruddin S. A review on the manufacturing defects of complex-shaped laminate in aircraft composite structures. *Int J Adv Manuf Technol* 2017;91:4081–94. doi:10.1007/s00170-017-0096-5.
- [25] Mukhopadhyay S, Jones MI, Hallett SR. Tensile failure of laminates containing an embedded wrinkle; numerical and experimental study. *Compos Part A Appl Sci Manuf* 2015;77:219–28. doi:10.1016/j.compositesa.2015.07.007.
- [26] Mukhopadhyay S, Jones MI, Hallett SR. Compressive failure of laminates containing an embedded wrinkle; experimental and numerical study. *Compos Part A Appl Sci Manuf* 2015;73:132–42. doi:10.1016/j.compositesa.2015.07.007.
- [27] Adams DO, Hyer MW. Effects of layer waviness on the compression strength of thermoplastic composite laminates. *J Reinf Plast Compos* 1993;12:414–29.
- [28] Xie N, Smith RA, Mukhopadhyay S, Hallett SR. A numerical study on the influence of composite wrinkle defect geometry on compressive strength. *Mater Des* 2018;140:7–20. doi:10.1016/j.matdes.2017.11.034.
- [29] Hu H, Cao D, Cao Z, Li S. Experimental and numerical investigations of wrinkle effect on failure behavior of curved composite laminates. *Compos Struct* 2021;261:113541. doi:10.1016/j.compstruct.2021.113541.

- [30] Xu X, Jones MI, Ali H, Wisnom MR, Hallett SR. Effect of out-of-plane wrinkles in curved multi-directional carbon/epoxy laminates. *Compos Sci Technol* 2020;197:108282. doi:10.1016/j.compscitech.2020.108282.
- [31] Journoud P, Bouvet C, Castanié B, Ratsifandrihana L. Experimental analysis of the effects of wrinkles in the radius of curvature of L-Shaped CFRP specimens on unfolding failure. *Compos - Part A Appl Sci Manuf* 2022:Under review.
- [32] Dassault Systemes. (2014). *Abaqus User Subroutines Reference Guide, Version 6.14*. Dassault Systemes Simulia Corp., Providence, RI, USA n.d.
- [33] Bouvet C, Castanié B, Bizeul M, Barrau JJ. Low velocity impact modelling in laminate composite panels with discrete interface elements. *Int J Solids Struct* 2009;46:2809–21. doi:10.1016/J.IJSOLSTR.2009.03.010.
- [34] Dubary N, Bouvet C, Rivallant S, Ratsifandrihana L. Damage tolerance of an impacted composite laminate. *Compos Struct* 2018;206:261–71. doi:10.1016/J.COMPSTRUCT.2018.08.045.
- [35] Serra J, Bouvet C, Castanié B, Petiot C. Scaling effect in notched composites: The Discrete Ply Model approach. *Compos Struct* 2016;148:127–43. doi:10.1016/j.compstruct.2016.03.062.
- [36] Bouvet C, Rivallant S, Barrau JJ. Low velocity impact modeling in composite laminates capturing permanent indentation. *Compos Sci Technol* 2012;72:1977–88. doi:10.1016/J.COMPSCITECH.2012.08.019.
- [37] Hongkarnjanakul N, Bouvet C, Rivallant S. Validation of low velocity impact modelling on different stacking sequences of CFRP laminates and influence of fibre failure. *Compos Struct* 2013;106:549–59. doi:10.1016/j.compstruct.2013.07.008.
- [38] Dassault Systemes. (2013). *Abaqus 6.14 –Analysis Users’s Guide: Volume IV: Elements*. Providence, Rhode Island. n.d.
- [39] Serra J, Bouvet C, Castanié B, Petiot C. Experimental and numerical analysis of Carbon Fiber Reinforced Polymer notched coupons under tensile loading. *Compos Struct* 2017;181:145–57. doi:10.1016/j.compstruct.2017.08.090.